Mass Loading and Stokes Number Effects in Steady and Unsteady Particle-laden Jets

M.Eng. Science Thesis

Richard J. Foreman
The University of Adelaide
The School of Mechanical Engineering
June 2008

Chapter 1

Introduction

1.1 Wider Significance

It is widely accepted that human activities, especially the combustion of fossil fuels, are the primary cause of global warming (IPCC, 2007). The combustion of fossil fuels are the dominant source of energy for industry, transportation and suburbia, which makes them integral to the functioning of society in its current form. Consequently, if the output of harmful emissions proceed at their current rate, the IPCC predicts a global average temperature rise of up to 4^oC by the year 2100. As a result, the planet may endure potentially damaging events such as rising sea levels from between 0.5 and 2m (due to both the thermal expansion of oceans as well as the melting of ice caps), reduced precipitation over most land areas, as well as increased droughts, heat waves and cyclone intensity.

The chief cause of global warming is predominantly due to the release of the greenhouse gas, CO_2, from the combustion of coal. Some ways to mitigate CO_2 emissions include the more effective and efficient use of fossil fuels, or their substitution for some renewable energy source, such as biofuels. The combustion of coal represents the most significant source of greenhouse gases

Figure 1.1: The contribution of CO2 to the atmosphere by the three fossil fuels in the past and in the future if current trends continue (adapted from Vernon, 2006).

because it is abundant and cheap compared with other sources of energy (e.g. Nuclear). In Figure 1.1 is a diagram indicating the relative contributions of atmospheric CO2 by coal, gas and oil 100 years prior and 150 years into the future assuming current lifestyle and combustion trends are maintained. From this figure it can be seen that by about 2050, gas and oil supplies would have peaked (although there are those that predict this to occur much earlier) and the excess energy requirements due to diminished gas and oil reserves are expected to have to be replaced with coal, contingent that other renewable energy sources are not used in place of fossil fuels.

Naturally, the use of coal in lieu of gas and oil is predicted to have devastating consequences for the planet. However, it is unlikely that renewable sources will play no role in the future. Other alternatives to renewable energy may encompass carbon offsets and sequestration techniques, as well as the focus in improving energy efficiency. Until there is an economic and political will to halt the dominant role fossil fuels have in satiating global energy requirements though, fossil fuels and especially coal, will continue to be an important source of energy and hence, CO2.

This leads to the wider aim of the following research. This research is expected to contribute to the body of knowledge concerning the combustion of pulverised fuel, whether that be coal or an alternative fuel such as biomass or waste. Knowledge of the fundamental physics driving these processes will facilitate their improved combustion performance and efficiency, thus helping reduce the output of harmful CO_2 emissions.

1.2 Multiphase flow

Prior to combustion in most industrial processes such as a coal fired power generation plant, the coal is milled into fine particles to be subsequently conveyed to the burner. The conveying and combustion of particle-laden flows is a practical realisation of the much broader field of multiphase flow. Multiphase flow falls within the discipline of fluid mechanics. Here, the fluid flow is complicated by the extra interactions and dynamics that arise as a result of the addition of at least one extra phase. A multiphase system may be a gas-liquid (e.g. sprays), gas-solid (e.g. fluidised beds), liquid-solid (e.g. slurries) or three-phase (e.g. bubbles in slurries) flow (Crowe *et al.*, 1998). The conveying and combustion of particles in air is a type of gas-solid flow. Also encountered in many power generation plants are gas-liquid flows such as the flow of liquid-vapour mixtures through boilers, condensers and even turbines. An understanding of the physics that govern multiphase flow processes is thus crucial for the optimal design of power generation plants and naturally, any other plant where multiphase flows are encountered.

However, a lack of understanding in the field of gas-solid flows has been attributed to the poor design performance in plants where the processing of solids is a significant aspect of operation. Merrow, Phillips and May (1981) found that plants such as these performed on average below their design capacity at approximately 35% greater than plants processing primarily liquids or gases. This was attributed to a poorer theoretical understanding of the behaviour of solids compared with gases or liquids. The trends found in that

study, while conducted more than 25 years ago, is believed to still reflect the current situation in industry today, despite the subsequent theoretical and technological advances in the field since then (DTI, 2004). For engineers to possess a greater capability to design and optimise the necessary plant, at least to standards comparable to gas and liquid processing plants, the understanding of the processing of solids, whether that be for conveying, combustion or any other purpose, must be improved.

The theory and experimental data in this thesis is presented in the context of a practical aim to improve combustion systems and so to ameliorate harmful emissions. Perhaps the simplest burner is an axisymmetric pipe jet, which is described below. The effect of the addition of solid particles (simulating pulverised coal in an industrial flame) to such a jet, termed a 'particle-laden jet', is the primary focus of this thesis. The effect of particles on the jet itself and the distribution of particles within the jet is of a fundamental importance to the performance of the flame, as this dictates the local air-fuel ratios and hence affects the combustion efficiency (Crowe, 2006) and also the production of most pollutants. Thus, there is a clear need to understand the effect of particles on the flow and the distribution of particles within the flow.

1.2.1 Gas-Solid Flows

Consider a spherical particle of diameter d_p, density ρ_p and volume V_p. The equation describing the motion of such a particle in a fluid is

$$\rho_p V_p \frac{d\widetilde{u}_p}{dt} = F_p, \tag{1.1}$$

where F_p is the force on the particle with instantaneous velocity, $\widetilde{u}_p$. In dilute gas-solid flows, the density of the solid phase is generally much greater than that of the gas phase and as a result, all forces, other than the drag force

D_F, may be neglected (Crowe *et al.*, 1998). In that case,

$$\rho_p V_p \frac{d\widetilde{u}_p}{dt} = D_F. \tag{1.2}$$

In the limit of very small particle Reynolds numbers, i.e.

$$Re_p = \frac{\rho \left|\widetilde{u} - \widetilde{u}_p\right| d_p}{\mu} < 1, \tag{1.3}$$

where $\widetilde{u}$ is the fluid velocity, ρ is the fluid density, and the drag coefficient, C_D is related to the Reynolds number by the linear relation (Munson *et al.*, 2002)

$$C_D = \frac{24}{Re}. \tag{1.4}$$

The equation of motion for a particle in this regime (the 'Stokes flow' regime) thus becomes (after rearranging)

$$\frac{d\widetilde{u}_p}{dt} = \frac{18\mu}{\rho_p d_p^2} f_d \left|\widetilde{u} - \widetilde{u}_p\right|. \tag{1.5}$$

The dimension of the ratio $\rho_p d_p^2/18\mu$ is seconds and is commonly known as the 'particle time scale', τ_p, and f_d is the drag factor. After the substitution of τ_p, then

$$\frac{d\widetilde{u}_p}{dt} = \frac{f_d}{\tau_p}(\widetilde{u} - \widetilde{u}_p). \tag{1.6}$$

The solution of this equation, assuming a constant fluid velocity (e.g. 1-dimensional channel flow), and initial conditions, $t = 0$ and $u_p = 0$, is

$$u_p = u\left[1 - exp\left(-\frac{t}{\tau_p}\right)\right]. \tag{1.7}$$

This equation shows that the particle timescale is a quantitative measure of the time ($t = \tau_p$) required for a particle with initial velocity, $u_p(t = 0) = 0$, to obtain a velocity of approximately 63% that of the fluid velocity.

For some flows of practical interest, the conditions of one-dimensionality, constant fluid velocity and $u_p(t = 0) = 0$ are not realistic, which means de-

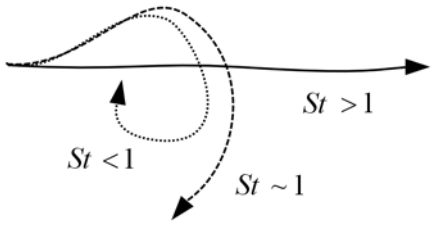

Figure 1.2: Conceptual realisation of the different regimes of St_o (adapted from Crowe *et al.*, 1988).

termining the precise position or velocity of a particle after time t is very difficult. Instead, the particle timescale is usually compared with some characteristic flow timescale, τ_f. The ratio of these timescales forms the important non-dimensional parameter, the Stokes number, where

$$St = \frac{\tau_p}{\tau_f}. \tag{1.8}$$

In essence, the Stokes number is a relative measure of the responsiveness of a particle to the state of the flow. Particles are usually classified into three broad regimes: $St > 1$ ('unresponsive'), $St \sim 1$ ('partially responsive') and $St < 1$ ('responsive'). Figure 1.2 illustrates the relative movement particles in each of these regimes relative to an eddy with some 'turnover' timescale, $\tau_f = l_e/u_e$, where l_e and u_e are the characteristic length and velocity scales of the eddy, respectively. While particles of $St < 1$ will follow the vortical eddy structure well, particles of larger St will possess entirely different trajectories from that of the eddy.

Two common ways of classifying the quantity of particles in a flow are the ratio of the masses of each phase, the 'loading', and the volumetric fraction. The mass loading is defined as

$$\phi = \frac{\dot{m}_p}{\dot{m}_f}, \tag{1.9}$$

where $\dot{m}_p$ is the solid phase mass flow rate and $\dot{m}_f$ is the gas phase mass flow rate. The volumetric fraction is defined as

$$\psi = N\frac{V_p}{V}, \tag{1.10}$$

where N is the number of particles and V is the fluid volume.

As the quantity of particles in a flow increases, their effect on the flow dynamics also increases. For example, if $\psi < 10^{-6}$, the addition of particles is sufficiently small that they will not bring about an appreciable alteration to the turbulence of the flow, i.e. 'one-way coupling' is closely approximated. On the other hand, if $\psi > 10^{-6}$, particles are found to affect the gas phase flow dynamics. One way this may happen is through 'turbulence modulation', which refers to the influence of the particles on the fluid turbulence (Crowe, 2000). For example, the timescale, τ_f of the ideal eddy described in Figure 1.2 may be increased by some damping action by the particles and this correspondingly changes St. Hence, the dispersion of the particles by the action of the fluid will be affected also, i.e. 'two-way coupling' (Elghobashi, 1994).

1.3 Single Phase Flow

Although the governing equations in gas-solid flows are still being debated, the Navier-Stokes equations are thought to describe the motion of single phase flows completely (Crowe *et al.*, 1998). The Reynolds averaged Navier-Stokes equations, for a Cartesian reference frame and a constant density system are (Rajaratnam, 1976)

$$\frac{\partial u}{\partial t} + u\frac{\partial u}{\partial x} + v\frac{\partial u}{\partial y} + w\frac{\partial u}{\partial z} = -\frac{1}{\rho}\frac{\partial p}{\partial x} + \nu\left(\frac{\partial^2 u}{\partial x^2} + \frac{\partial^2 u}{\partial y^2} + \frac{\partial^2 u}{\partial z^2}\right) - \left(\frac{\partial \overline{u'^2}}{\partial x} + \frac{\partial \overline{u'v'}}{\partial y} + \frac{\partial \overline{u'w'}}{\partial z}\right) \tag{1.11}$$

$$\frac{\partial v}{\partial t} + v\frac{\partial u}{\partial x} + v\frac{\partial v}{\partial y} + w\frac{\partial v}{\partial z} = -\frac{1}{\rho}\frac{\partial p}{\partial y} + \nu\left(\frac{\partial^2 v}{\partial x^2} + \frac{\partial^2 v}{\partial y^2} + \frac{\partial^2 uv}{\partial z^2}\right) - \left(\frac{\partial \overline{u'v'}}{\partial y} + \frac{\partial \overline{v'^2}}{\partial x} + \frac{\partial \overline{v'w'}}{\partial z}\right), \tag{1.12}$$

$$\frac{\partial w}{\partial t} + w\frac{\partial u}{\partial x} + v\frac{\partial w}{\partial y} + w\frac{\partial w}{\partial z} = -\frac{1}{\rho}\frac{\partial p}{\partial z} + \nu\left(\frac{\partial^2 w}{\partial x^2} + \frac{\partial^2 w}{\partial y^2} + \frac{\partial^2 w}{\partial z^2}\right) - \left(\frac{\partial \overline{u'w'}}{\partial x} + \frac{\partial \overline{v'w'}}{\partial y} + \frac{\partial \overline{w'^2}}{\partial z}\right). \tag{1.13}$$

Here, u, v and w are the time averaged velocity components in the x, y and z directions respectively, primes and over bars denote fluctuating and averaged quantities respectively, p is the static pressure and ν is the kinematic viscosity. On the left hand side, the first term is the unsteady term followed by the inertial terms. On the right are the pressure, viscous and Reynolds stress terms.

The Reynolds 'stress' (e.g. $-\rho\overline{u'v'}$) arises from the Reynolds averaging of the original Navier-Stokes equations. It can be physically described as the transfer of momentum between 'clumps' of fluid moving with different velocity. For example, in a turbulent shear flow with mean velocity $u = u(y)$, drawn in Figure 1.3, a clump of fluid with velocity $u' < 0$ will be transported upwards (positive y) with velocity $v' > 0$ and for clumps of fluid $u' > 0$, they will be transported downwards with velocity $v' < 0$. The Reynolds stress in this scenario will amount to $\overline{u'v'} < 0$.

With the introduction of the continuity equation,

$$\frac{\partial u}{\partial x} + \frac{\partial v}{\partial y} + \frac{\partial w}{\partial z} = 0 \tag{1.14}$$

in addition to equations 1.11 to 1.13, it can be seen that there are 10 unknowns, yet only 4 equations. It is the endeavour of turbulence modeling to

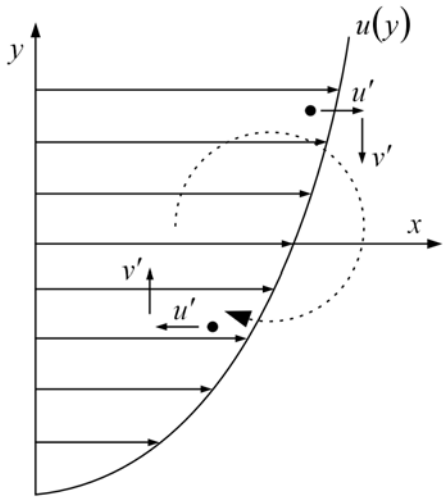

Figure 1.3: Two-dimensional shear flow indicating the correlation of fluid 'clumps'.

find a generalised set of closed equations. For relatively simple cases, such as the axisymmetric turbulent jet to be considered next, semi-empirical solutions are attainable if a number of assumptions are invoked. However, such solutions are applicable only for that type of flow and boundary conditions.

1.4 Turbulent Jets

1.4.1 Steady axisymmetric and plane turbulent jets

A simple turbulent axisymmetric jet, with initial momentum, M and density, ρ issuing from a pipe of some diameter, D is a particular class of free shear flow. Turbulent jets, in contrast to laminar ones, are notable for the myriad of length scales, the smallest being the Kolmogrov scale, the largest, an order of magnitude equal with the width of the jet as seen in the instantaneous image of a water jet marked with dye, Figure 1.4. The turbulence results in the rapid exchange of momentum within the jet, and between the jet and

NOTE: This figure is included on page 10 of the print copy of the thesis held in the University of Adelaide Library.

Figure 1.4: An instantaneous image showing that a wide range of turbulent scales are present in a water jet marked by dye, Re = 2.5 ×103 (Dimotakis et al., 1983).

ambient flow, up to length scales the order of the jet diameter. In contrast, the mixing and momentum exchange in laminar jets occurs at a molecular scale, described by the fluid viscosity. Differences between the two can be quantified in terms of the famous dimensionless parameter, the Reynolds number, which for a jet, is defined as

$$RE = \frac{UD}{\mu} \qquad (1.15)$$

Here, U is the jet bulk exit velocity and μ is the dynamic viscosity. Physically, the Reynolds number expresses a ratio of inertial forces to viscous forces in any type of flow. Laminar jets possess low Reynolds numbers which infers that viscous forces are more dominant than inertial forces.

Shown in Figure 1.5 is a schematic diagram of the important parameters of the time averaged flow in a turbulent axisymmetric jet. In the initial region is the potential core, the region where the velocity is constant across the width of the exit diameter. This potential core is only strictly present for smooth contraction jets. Differences in exit profiles (as well as other properties downstream of the exit) are found between smooth contractions and pipe jets (Mi et al., 2001). However, for simplicity, a constant exit profile

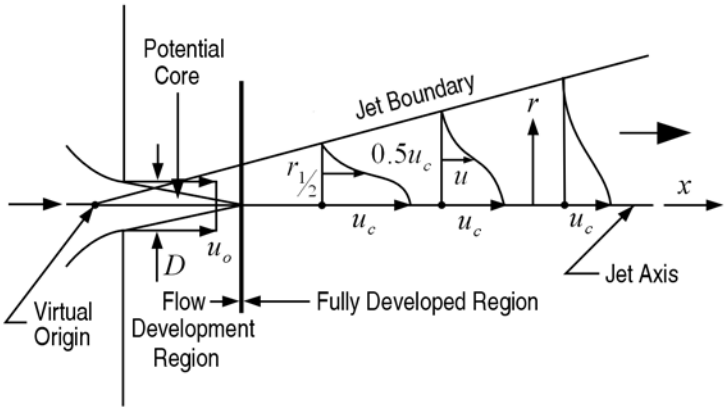

Figure 1.5: Key time-averaged features of a turbulent jet (adapted from Rajaratnam, 1976).

will be assumed here. At the tip of the potential core, the shear layers merge and after a brief transition region, the fully developed region begins. In that region, the mean velocity profile approximates a Gaussian profile, with the maximum velocity occurring on the jet axis. As one proceeds downstream, the profiles will spread to greater radial extents as seen by the ever increasing jet boundary. The centreline velocity, u_c, will correspondingly decrease as x increases. The spread of the jet is usually defined in terms of the half width, $r_{1/2}$, which is the distance between the centreline and some point where the velocity is half that of u_c. The use of the half width is preferred since the actual jet boundary can be ambiguous and many more measurements must be performed for it to be detected.

When analysing a flow of this type, a number of assumptions can be made to simplify the Navier-Stokes equations 1.11 to 1.13. The first such assumption is of axisymmetry for the case of a round jet and an infinitely long thin section for the case of a plane jet. In both cases, the number of dimensions is reduced to two, which means the number of variables is reduced by 4 by the removal of equation 1.13. Following Rajaratnam (1976) a plane jet will be analysed first and this will be extended to the case of a round or axisymmetric jet. The second simplification is an assumption of steadiness,

which implies the time-averaged velocity is constant. Hence, the term $\partial()/\partial t$ is removed from equations 1.11 and 1.12. With these simplifications, the system of equations are as follows:

$$u\frac{\partial u}{\partial x} + v\frac{\partial u}{\partial y} = -\frac{1}{\rho}\frac{\partial p}{\partial x} + \nu\left(\frac{\partial^2 u}{\partial x^2} + \frac{\partial^2 u}{\partial y^2}\right) - \left(\frac{\partial \overline{u'^2}}{\partial x} + \frac{\partial \overline{u'v'}}{\partial y}\right), \tag{1.16}$$

$$u\frac{\partial v}{\partial x} + v\frac{\partial v}{\partial y} = -\frac{1}{\rho}\frac{\partial p}{\partial y} + \nu\left(\frac{\partial^2 v}{\partial x^2} + \frac{\partial^2 v}{\partial y^2}\right) - \left(\frac{\partial \overline{u'v'}}{\partial x} + \frac{\partial \overline{v'^2}}{\partial y}\right) \tag{1.17}$$

and (continuity)

$$\frac{\partial u}{\partial x} + \frac{\partial v}{\partial y} = 0. \tag{1.18}$$

One of the fundamental concepts of modern fluid mechanics is the boundary layer assumption (Kundu & Cohen, 1999) which states that streamwise or axial (the x direction) variations within the boundary layer are insignificant relative to variations perpendicular (the y direction) to a thin layer as illustrated in the idealised flow over a flat plate in Figure 1.6. This implies that

$$\frac{\partial}{\partial x} \ll \frac{\partial}{\partial y}. \tag{1.19}$$

Further, u is much larger than v, hence

$$u \gg v. \tag{1.20}$$

A jet is a class of shear flow which, because of the absence of boundaries, is regarded as a *free* shear flow.

As a result, boundary-layer like approximations can be made to reduce equations 1.16 and 1.17 to

$$u\frac{\partial u}{\partial x} + v\frac{\partial u}{\partial y} = -\frac{1}{\rho}\frac{\partial p}{\partial x} + \nu\frac{\partial^2 u}{\partial y^2} - \frac{\partial \overline{u'v'}}{\partial y} \tag{1.21}$$

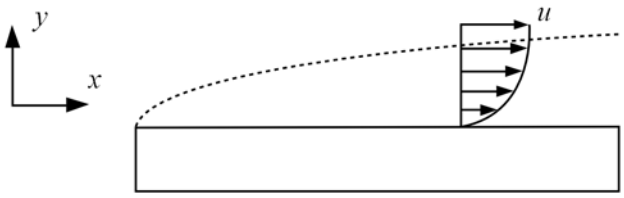

Figure 1.6: Flow over a flat plate. Dashed line denotes the hypothetical boundary layer.

and

$$0 = -\frac{1}{\rho}\frac{\partial p}{\partial y} - \frac{\partial \overline{v'^2}}{\partial y}. \tag{1.22}$$

The pressure gradient $\frac{\partial p}{\partial x}$ can be found by integrating equation 1.22 to give

$$p = p_\infty - \rho\overline{v'^2}, \tag{1.23}$$

where p_∞ is the ambient pressure. The quantity $\rho\overline{v'^2}$ is maximum at the jet centreline (George, 1990), which implies there is a pressure gradient toward the centre of the jet and as a result, ambient fluid is entrained toward the centreline. However, p can be approximated as being constant, but it does vary according to the imposed conditions from outside the jet boundary (Kundu & Cohen, 1999). Hence, equation 1.21 can be approximated as

$$u\frac{\partial u}{\partial x} + v\frac{\partial u}{\partial y} = \nu\frac{\partial^2 u}{\partial x^2} - \frac{\partial \overline{u'v'}}{\partial y}, \tag{1.24}$$

which can also be written as

$$u\frac{\partial u}{\partial x} + v\frac{\partial u}{\partial y} = \frac{1}{\rho}\frac{\partial}{\partial y}\left(\mu\frac{\partial u}{\partial y} - \rho\overline{u'v'}\right). \tag{1.25}$$

Written in this way, the terms $\mu\frac{\partial u}{\partial y}$ and $-\rho\overline{u'v'}$, the laminar and Reynolds shear stresses, are revealed. An implication of the assumption of a high Reynolds number is that turbulent stresses are much higher than the laminar

stresses. If the laminar stresses are neglected, equation 1.25 becomes

$$u\frac{\partial u}{\partial x} + v\frac{\partial u}{\partial y} = -\frac{1}{\rho}\frac{\partial \rho\overline{u'v'}}{\partial y}, \tag{1.26}$$

while continuity remains as

$$\frac{\partial u}{\partial x} + \frac{\partial v}{\partial y} = 0. \tag{1.27}$$

These set of equations are nearly closed since there are three unknowns and two equations. Another concept can be used to further reduce the complexity of these equations. The phenomena of profiles of some physical property collapsing onto one another, once normalised with some characteristic scale, is called 'self-preservation'. This occurs in the fully developed region of a turbulent jet. Shown in Figure 1.7(a) are radial profiles in the fully developed region of an axisymmetric jet at a number of axial locations. If these profiles are normalised by the characteristic velocity scale, the centreline velocity u_c, and by a length scale, the half widths $r_{1/2}$, then it is found that the profiles collapse onto a single curve as is shown in Figure 1.7(b). The 'self-similar' velocity profiles indicate the velocity field is now independent of the axial or streamwise direction. Physically, it has been said (George, 1989) that self-similarity implies a dynamic equilibrium of all the terms controlling the motion. As a result, the rate of change of each dynamic term in the equation of motion is equal (further meaning the flow is absent of an external force).

The absence of an external force is shown by integrating equation 1.26 with respect to y from either boundary of the jet ($-\infty$ to $+\infty$). Firstly, rearranging equation 1.26 such that

$$u\frac{\partial u}{\partial x} + \frac{\partial uv}{\partial y} - u\frac{\partial v}{\partial y} = -\frac{1}{\rho}\frac{\partial \rho\overline{u'v'}}{\partial y}, \tag{1.28}$$

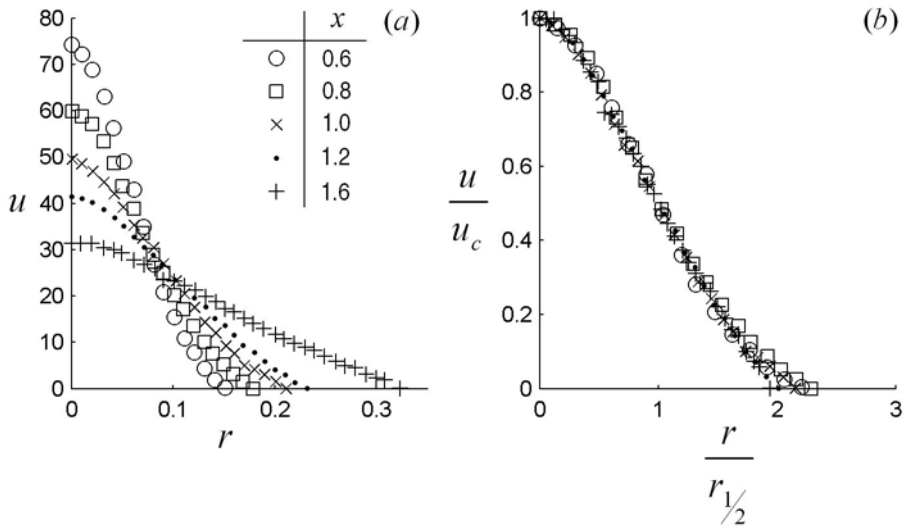

Figure 1.7: (a) Radial velocity profiles at a number of axial locations and (b) those profiles normalised by u_c and $r_{1/2}$ in a round jet (Rajaratnam, 1976).

and using continuity equation 1.27, then

$$\frac{\partial v}{\partial y} = -\frac{\partial u}{\partial x}. \tag{1.29}$$

Thus

$$u\frac{\partial u}{\partial x} + \frac{\partial uv}{\partial y} + u\frac{\partial u}{\partial x} = -\frac{1}{\rho}\frac{\partial \rho\overline{u'v'}}{\partial y} \tag{1.30}$$

and therefore

$$\frac{\partial (u^2)}{\partial x} + \frac{\partial uv}{\partial y} = -\frac{1}{\rho}\frac{\partial \rho\overline{u'v'}}{\partial y}. \tag{1.31}$$

Integrating this equation gives

$$\frac{d}{dx}\int_0^\infty u^2 dy + 2[uv]_0^\infty = -2[\overline{u'v'}]_0^\infty. \tag{1.32}$$

Assuming the following boundary conditions, $u(y=\infty)=0, v(y=0)=0$, gives $[uv]_0^\infty = 0$. The following graph of measurements of the turbulent shear stress in an axisymmetric jet shows (Figure 1.8) that $\overline{u'v'}$ is zero along the jet axis, rises to a maxima at $r/x \approx 0.17$, then falls to zero as the transverse coordinate y, or in this case r for cylindrical coordinates, goes to infinity. A

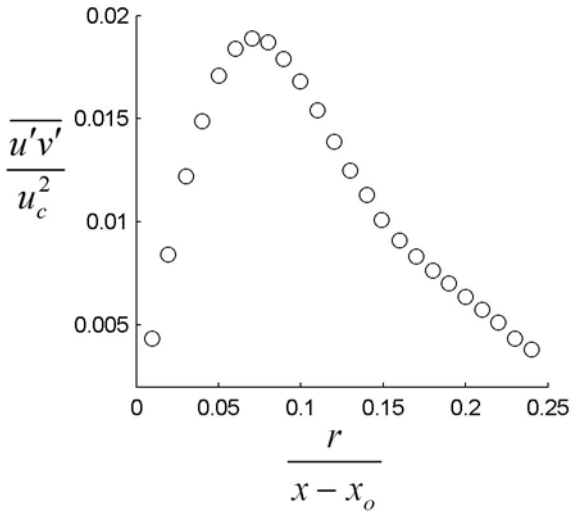

Figure 1.8: Turbulent shear stress for a round jet according to Hussein *et al.* (1994)

similar result is found in a plane jet. Therefore, $\overline{u'v'}(y=0)$ and $\overline{u'v'}(y=\infty)$, thus reducing equation 1.32 to

$$\frac{d}{dx}\int_0^\infty u^2 dy = 0, \tag{1.33}$$

which shows that the momentum flux (M/ρ) is conserved in the axial (x) direction.

The concept of self-similarity can be represented (Pope, 2000) by a function F, such that

$$F(x,r) = F(x,\xi)F_o(x), \tag{1.34}$$

where $\xi = r/r_l$ and $F_o(x)$ is some characteristic scale. Here, r is the radial direction and is normalised by some scale in that direction, r_l. If it can be shown that $F(x,\xi)$ is independent of x, (as was done in Figure 1.7), then

$$F(x,\xi) = f(\xi), \tag{1.35}$$

where f is some function and $r_l = r_{1/2}$. Substituting the velocity, u, for the

arbitrary function F in equations 1.34 and 1.35 then,

$$u(x,r) = f(\xi)u(x,0) = f(\xi)u_c. \tag{1.36}$$

Rearranging equation 1.36 in terms of ξ gives

$$\frac{u}{u_c} = f(\xi). \tag{1.37}$$

Equation 1.37 describes the function f as seen in the scaled velocity profiles of Figure 1.7.

The axial momentum equation (equation 1.26) is now converted to cylindrical coordinates as this simplifies the analysis of an axisymmetric jet:

$$u\frac{\partial u}{\partial x} + v\frac{\partial u}{\partial r} = \frac{1}{\rho}\frac{1}{r}\frac{\partial r\tau}{\partial r}, \tag{1.38}$$

where $\tau = \rho\overline{u'v'}$. The turbulent shear stress, when normalised by the squared centreline velocity, is equal to the function h where

$$\frac{\tau}{\rho u_c^2} = h(\xi). \tag{1.39}$$

If similarity relations 1.39 and 1.37 are substituted into equation 1.38, then it follows that

$$\frac{1}{\rho}\frac{1}{r}\frac{\partial r\tau}{\partial r} = \frac{1}{r}\frac{\partial(ru_c^2h)}{\partial r} = \frac{u_c^2}{r_{1/2}}H(\xi), \tag{1.40}$$

where $H(\xi) = h/\xi + \partial g/\partial\xi$.

Further from Rajaratnam (1976), the quantities on the left hand side of equation 1.38 are

$$u\frac{\partial u}{\partial x} = u_c\frac{du_c}{dx}f^2 - \frac{u_c^2\frac{dr_{1/2}}{dx}}{r_{1/2}}\xi f\frac{df}{d\xi} \tag{1.41}$$

and

$$v\frac{\partial u}{\partial r} = \frac{u_c^2\frac{dr_{1/2}}{dx}}{r_{1/2}}\frac{df}{d\xi}\frac{F_1}{\xi} - u_c\frac{du_c}{dx}\frac{df}{d\xi}\frac{F_2}{\xi} \tag{1.42}$$

where $F_1 = \int_0^\xi \xi^2(df/d\xi)d\xi$ and $F_2 = \int_0^\xi \xi f d\xi$. If equations 1.40 to 1.42 are

inserted into 1.38, then it is found that

$$H(\xi) = \frac{r_{1/2}}{u_c}\frac{du_c}{dx}\left[f^2 - \frac{df}{d\xi}\frac{F_2}{\xi}\right] + \frac{dr_{1/2}}{dx}\left[\frac{df}{d\xi}\frac{F_1}{\xi} - \xi f\frac{df}{d\xi}\right]. \tag{1.43}$$

In this equation, $H(\xi)$ is independent of x and the terms in the square brackets are independent of x because f, F_1 and F_2 are all independent of x. It must follow then that $\frac{r_{1/2}}{u_c}\frac{du_c}{dx}$ and $\frac{dr_{1/2}}{dx}$ must be independent of x. Therefore, let

$$\frac{dr_{1/2}}{dx} = \text{constant}, \tag{1.44}$$

which implies (after integration) that $r_{1/2} \propto x$, and

$$\frac{r_{1/2}}{u_c}\frac{du_c}{dx} = \text{constant}. \tag{1.45}$$

Equation 1.45 is dealt with below.

The relationship between u_c and $r_{1/2}$ is found from the conservation of momentum flux, equation 1.33, which, after substitution of f and ξ gives

$$\frac{d}{dx}u_c^2 r_{1/2}^2 \int_0^\infty f^2 \xi d\xi = 0. \tag{1.46}$$

Since $\int_0^\infty f^2\xi d\xi$ is constant, then

$$u_c r_{1/2} = \text{constant} \tag{1.47}$$

and hence $u_c \propto 1/r_{1/2}$ and from equation 1.44, $u_c \propto 1/x$. Substituting $u_c \propto 1/x$ into equation 1.45 gives $r_{1/2} \propto x$, consistent with equation 1.44.

In conclusion, in an axisymmetric turbulent jet, the centreline velocity and half width are inversely and directly proportional to x, respectively. Non-dimensionalising u_c and $r_{1/2}$ gives

$$\frac{u_o}{u_c} = K_1\frac{x}{D} \tag{1.48}$$

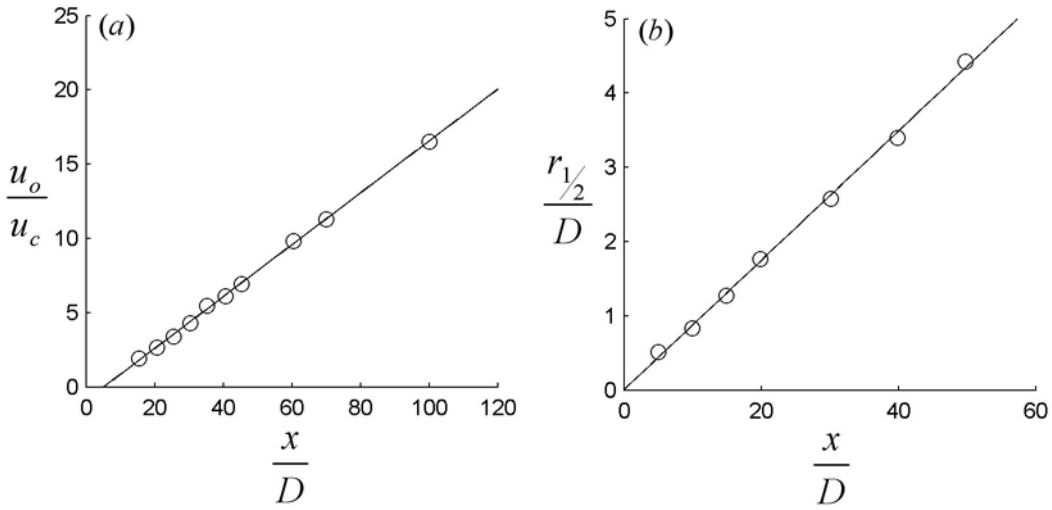

Figure 1.9: (a) Centreline velocity, u_c, in a axisymmetric jet measured by Hussein *et al.* (1994) and (b) half width, $r_{1/2}$, measured by Xu and Antonia (2002).

and

$$\frac{r_{1/2}}{D} = K_2 \frac{x}{D}. \tag{1.49}$$

Here, K_1 is the centreline decay coefficient and K_2 is the spreading coefficient.

These results have been supported by experimental data. Shown in Figure 1.9 are the linear dependence of u_o/u_c and $r_{1/2}$ on x, as reported by Hussein *et al.* (1994) and Xu and Antonia (2002). In Figure 1.9, it can be seen that the line of best fits through u_o/u_c and $r_{1/2}$ do not pass through the origin. The distance between the $x-$intercept and the actual origin is called the virtual origin. This will be ignored here for the purposes of simplicity.

1.4.2 Particle-laden axisymmetric jets

The addition of solid particles of some diameter, d_p to a turbulent jet will alter the gas phase mean velocity field and turbulent structure with respect to a single phase jet. Hardalupas *et al.* (1989) estimate that alterations to the mean velocity field will occur if the mass loading at the orifice exit,

$\phi_o \gtrsim 0.1$. The exit mass loading is defined as

$$\phi_o = \frac{\dot{m}_p}{\dot{m_{fo}}}, \tag{1.50}$$

where $\dot{m}_p$ is the solid phase mass flow rate and $\dot{m_{fo}}$ is the gas phase exit mass flow rate.

In the pioneering experimental work of Laats (1966), the effect of ϕ_o on the gas phase centreline mean velocity and half width of a turbulent axisymmetric jet was reported and is reproduced in Figure 1.10. Budilarto (2003), almost 40 years later, reported the same trend for the gas phase centreline velocity (Figure 1.11). His measurements were conducted with a Laser Doppler Anemometer, while those of Laats were measured using an isokinetic suction tube and rotameter arrangement. A brief review of these experimental techniques are included below. Other well known experimental works that report trends similar to that displayed in Figures 1.10 and 1.11, are those by Modarress *et al.* (1984a,b), Shuen *et al.* (1985), Tsuji *et al.* (1988), Hardalupas *et al.* (1989), Sheen *et al.* (1994), Fan *et al.* (1997) and others. The physical mechanisms responsible for the reduction in centreline decay and spreading rates, as displayed in Figures 1.10 and 1.11, are usually attributed to interphase momentum transfer and turbulence damping (e.g. Fleckhaus *et al.*, 1987).

The effect of particle mass loading ϕ_o on the gas phase centreline velocity, u_c and on the velocity half width, $r_{1/2}$ has been considered previously by Melville and Bray (1979). They began their analysis of particle-laden jets by writing the gas phase velocity distribution as the following function of dimensionless parameters:

$$\frac{u}{u_o} = f_n\left(\frac{x}{D}, \frac{r}{D}, Re, \phi_o, St_o\right), \tag{1.51}$$

where u is the time-averaged axial component of the gas phase velocity and r is the radial distance from the jet axis. The Reynolds number, $Re = \rho U D/\mu$, is defined using the bulk mean exit velocity U, the gas phase density ρ and

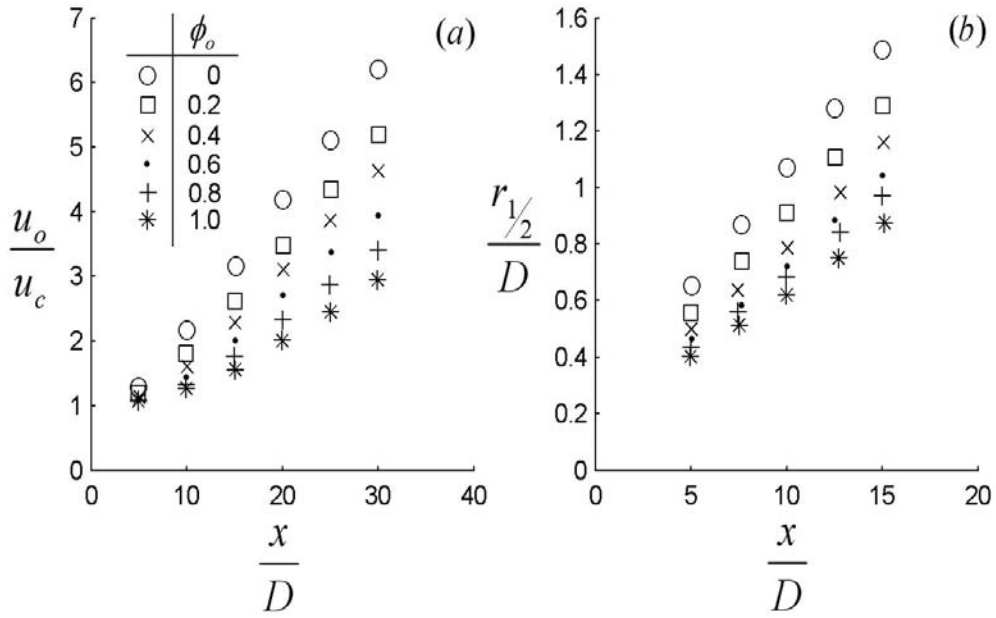

Figure 1.10: The dependence (a) of the mean centreline gas phase velocity and (b) half width reported by Laats (1966). $St_o = 19$.

NOTE: This figure is included on page 21 of the print copy of the thesis held in the University of Adelaide Library.

Figure 1.11: Gasphase centreline velocity as reported by Budilarto (2003). $St_o = 3$.

dynamic viscosity, μ. The Stokes number at the exit is defined as

$$St_o = \frac{\rho_p d_p^2 U}{18\mu D}, \tag{1.52}$$

where ρ_p is the particle density and d_p is the mean particle diameter. Initially, Melville and Bray neglect both Reynolds and Stokes numbers effects and they write the gas-phase centreline velocity as

$$\frac{u_o}{u_c} = K_1 \left(\frac{x}{D}\right) a(\phi_o) \tag{1.53}$$

and the gas-phase velocity half width as

$$r_{1/2} = K_2(x) b(\phi_o), \tag{1.54}$$

where a and b are functions of ϕ_o. Melville and Bray propose that a and b are exponential functions, giving

$$\frac{u_o}{u_c} = K_1 \frac{x}{D} e^{-0.69\phi_o} \tag{1.55}$$

and

$$\frac{r_{1/2}}{D} = K_2 \frac{x}{D} e^{-0.69\phi_o}. \tag{1.56}$$

Their scaling of the gas-phase centreline velocity and half width as reported by Laats (1966) are reproduced in Figure 1.12. While the correlations for both u_o/u_c and $r_{1/2}$ are strong, Melville and Bray acknowledge that a physical justification for their exponential scaling is not forthcoming. Measurements published since Melville and Bray (1979) provide further insight into the effect of particles on the mean and turbulent properties of a particle-laden jet. However, no other scaling approach has since been presented, which leads to a primary aim of this thesis. This is to obtain new scaling factors for gas phase centreline velocity and half width measurements published prior to (i.e. Laats, 1966) and since (i.e. Shuen *et al.*, 1983) Melville and Bray (1979). As opposed to the exponential scaling factors proposed by Melville and Bray (1979), power-law scaling factors are presented

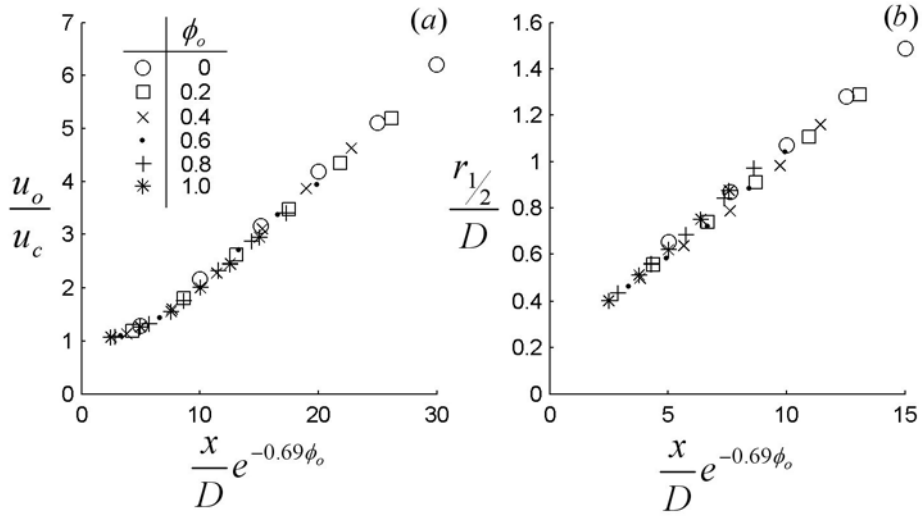

Figure 1.12: Melville and Bray's correlation of Laats' (1966) gas phase centreline velocity (a) and half width data (b), based on equations 1.55 and 1.56, respectively.

in chapter 2 for all previously published data sets which encompass a range of exit Stokes numbers.

The reported measurements of other jet properties such as jet entrainment, concentration and mass flux exhibit similar trends to the gas phase velocity. That is, jet entrainment, the spread of mass concentration and mass flux are all decreasing functions of ϕ_o. For example, both the centreline mass flux, $\dot{m}_{p,c}$, and half width $\dot{m}_{p,1/2}$ are shown in Figure 1.13 and reported by Laats and Frishman (1970) for $St_o = 18$, illustrate this. However, the mass flux decay and spreading rates are not linear as they were with the gas phase velocity. An exponential scaling of mass flux data was also proposed by Melville and Bray (1979). Likewise with gas phase velocity measurements, no scaling of entrainment, concentration or mass flux measurements have been reported since. The scaling of these aspects of particle-laden jets will also be addressed in Chapter 2, following the scaling of gas phase velocity measurements.

Whereas Figure 1.13 reports only a variation of mass flux with ϕ_o,

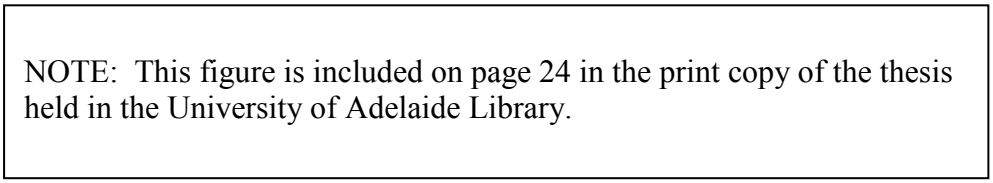

Figure 1.13: (a) Solid phase centreline mass flux and (b) half widths as reported by Laats and Frishman (1970). $St_o = 18$.

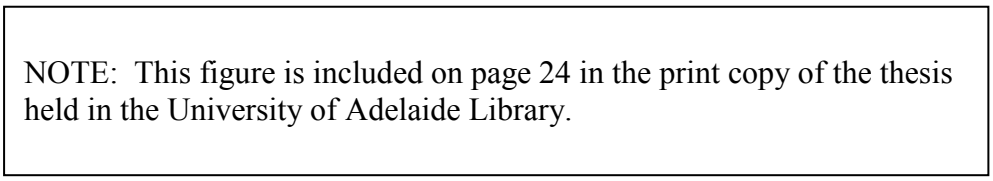

Figure 1.14: Centreline mass flux measurements as reported by Laats and Frishman (1970). $Ø_o = 0.3$.

Figure 1.14 illustrates different effects for a variation in St_o. For example, centreline mass flux measurements at low Stokes numbers (i.e. $St_o = 5$, 18) exhibit an increase in centreline concentration downstream of the jet exit, denoted the 'pinch-effect' after Frishman *et al.* (1997). The pinch-effect was originally attributed to the Magnus effect (Laats and Frishman, 1970) but, recently, numerical simulations have determined the effect to be much more complex, with the history of the particle motion within the pipe a factor that must be considered among other things (Frishman *et al.*, 1997). While the pinch-effect is detected for relatively low Stokes numbers, it is absent for larger Stokes numbers (i.e. $St_o = 42$, Figure 1.14). Rather, there is a rapid reduction in $\dot{m}_{p,c}$ immediately downstream of the jet exit. Beyond the initial region and pinch-effect, the decay of $\dot{m}_{p,c}$ is greater for the smaller particles ($St_o = 5$) compared with the larger ones ($St_o = 42$). Also, the shape of the concentration profiles at the jet exit are also dependent on the Stokes number (Frishman *et al.*, 1997). For example, a concave concentration profile, with the minimum value located on the nozzle centreline, is detected for low Stokes numbers. All these Stokes numbers effects, the pinch-effect, the centreline decay and exit profile shape are investigated further in Chapter 3. These effects will be assessed by measurements of the time-averaged particle distributions.

Measurements of particle distributions, (i.e. Planar scattering measurements, see section 1.5.3), have been used in the past to discern important information concerning the instantaneous location of particles relative to the jet structure (e.g. Longmire and Eaton, 1992). In this study, the time-averaged distribution of particles will be measured to investigate the variation of the Stokes number and mass loading. The Stokes number effects as briefly detailed in the previous paragraph will investigated. However, primarily, the scaling of particle distributions will be investigated also. These measurements and their subsequent scaling of mass loading effects will be reported in Chapter 3. As with mass flux data, no scaling of these measurements have been reported to date.

Figure 1.15: A simplified schematic representation of the PJ nozzle and the emerging precessing jet flow (Nathan et al., 2006).

1.4.3 Unsteady jets: The precessing and triangular oscillating jets

Unsteady jets are even more complicated than the steady axisymmetric jets discussed above. Many of the simplifying assumptions that facilitated a semi-empirical dimensional solution for the axisymmetric jet (Equations 1.48 and 1.49), such as, obviously, steadiness, two-dimensionality and selfpreservation, are inapplicable for the unsteady jets to be considered here, at least in the near field. The precessing jet (PJ), first described in Nathan (1988), is an unsteady jet that is produced by a nozzle such as that shown in Figure 1.15. From that diagram, it can be seen that the flow emerges at an angle to the centreline and 'precesses' periodically in the azimuthal direction. A hypothesised mechanism (Kelso, 2001) driving the external jet precession is the asymmetric azimuthal distribution of vortices that generate a pressure differential within the chamber, inducing unsteady attachment to the chamber wall after sudden expansion through the orifice, d1.

Important properties that distinguish the PJ from a steady jet are an increased near field spread (Parham, 2000), as well as larger jet structures (Newbold et al., 1997). For combustion applications, this has resulted in an increased flame volume, luminosity, residence time and stability (Parham,

2000, Smith, 2000). Under certain conditions, a PJ nozzle offers advantages over a standard burner because it gives an increase in heat transfer (improved efficiency) and reduced NO_x emissions (Smith, 2000). However, these benefits come at the expense of a relatively high driving pressure. While this is readily available in natural gas plants, it is beyond the attainable limits of standard plant fans, especially those plants that are fueled by a solid such as coal. This is important since the majority of say, cement kilns and furnaces, specific applications where unsteady nozzle are proposed to be used, use coal as their primary fuel. To address this problem, the triangular oscillating jet (OJ) nozzle was developed. This also generates a large scale oscillation of the emerging jet but at a comparatively lower driving pressure (Lee *et al.*, 2003). Its construction is similar to the PJ nozzle, but as its name suggests, the circular orifice is replaced with a triangle. Importantly for the purposes of this work, there are some differences in the emerging flow as well. The most basic difference is that the absolute mean spread of the flow from an OJ nozzle is less than a PJ nozzle (Lee *et al.*, 2003).

No measurements of the effect of oscillating jet momentum and the exit mass loading on particle distributions has been conducted. Furthermore, a comparison with existing measurements in a particle-laden precessing jet (Birzer *et al.*, 2005) is yet to be conducted. Hence, a planar imaging technique similarly to that used for a particle-laden steady jets in Chapter 3, is used to measure particle distributions in a triangular oscillating jet flow. These are presented in Chapter 4 and compared with similarly obtained PJ measurements.

1.5 Measurement Techniques

The measurement techniques used to obtain some of the published data presented above, such as gas and solid phase velocities, as well as the solid phase mass flux, are discussed in this section. Some of the concepts presented here are also related to the measurement methods applied to obtain the data

Figure 1.16: Doppler shift of scattered light from a moving particle (Crowe *et al.*, 1998)

presented in Chapters 3 and 4, such as the dependence of scattered light intensity on particle diameter. Finally, a justification for these measurements technique is provided.

1.5.1 Laser Doppler Anemometry, LDA

Velocity measurements of both phases in particle-laden jets are most commonly obtained with a Laser Doppler Anemometer (LDA). The basic components of a LDA setup are displayed in Figure 1.16. Shown is a laser emitting light of frequency, f_s in the direction of the unit vector $\vec{k}$. Laser light is scattered by a particle moving with velocity, $\widetilde{u}_p$, and subsequently observed by a photodetector. As a consequence of the Doppler effect, the frequency of scattered light as measured by the photodetector is

$$f_d = f_s \frac{1 - \frac{\widetilde{u}_p \cdot \vec{l}}{c}}{1 - \frac{\widetilde{u}_p \cdot \vec{k}}{c}}, \tag{1.57}$$

where c is the speed of light. This equation accounts for the modulation of the laser light as scattered by the moving particle and the moving particle relative to the photodetector.

Figure 1.17: Typical LDA setup detecting backscattered light. The fringe pattern of spacing Δx, created by the intersection of the two beams is shown along with the detected photo-detector signal of period T_D (adapted from Sorensen, 2005).

The scattered light frequency, f_d in the setup shown in Figure 1.16 is too high to be resolved by a photodetector. Instead, a laser beam may be split into two, and subsequently directed into an interference region which creates a fringe pattern as shown in Figure 1.17 of spacing Δx, where

$$\Delta x = \frac{\lambda}{2 \sin \frac{\theta}{2}}. \tag{1.58}$$

Here, λ is the laser wavelength and θ is the angle between the intersecting beams. The particle velocity is found from the measured signal frequency or period, T_D, so that

$$u_p = \frac{\Delta x}{T_D}. \tag{1.59}$$

Here, u_p is the particle velocity perpendicular to the axis of the intersecting beams (see Figure 1.17).

The intensity of light scattered by the particle is dependent on the laser light incident intensity, wavelength and polarisation, particle diameter and index of refraction and the detected scattering angle. If all variables, other than the particle diameter are held constant, the scattered intensity, as displayed in Figure 1.18 is proportional to the square of the diameter of larger

Figure 1.18: Dependence of scattering intensity on particle size for incident intensity = $10^7 \mathrm{W/m^2}$, detector angle with incident light beam = 15°, receiving solid aperture angle = 10° and complex refractive index = 1.5 (Crowe *et al.*, 1998)

particles. Crowe *et al.* (1998) used Mie scattering theory (see van de Hulst, 1981) to generate this plot.

The dependence of scattered light intensity on particle diameter is sometimes used to discriminate LDA measurements of the gas phase from that of the solid phase phase. In two phase flows, seeding particles with a Stokes number much less than one are assumed to be representative of gas phase velocities. For example, in gas flows, seeding particles will have a diameter of $O(1)\mu$m. The solid phase, having a much larger diameter, say of $O(100)\mu$m, scatters more intense light and hence, this type of signal can be identified as scattered by the solid phase. However, errors are introduced by the detection of larger particles passing through the edge of the interference region so that the signal amplitude from a large particle may appear as if it were scattered from a seeder. This error may be limited though if particles with a much larger velocity difference from the gas are used so that the velocities may be separated out (Sheen *et al.*, 1994). Another way to discriminate between

the phases is to use a Phase Doppler Anemometry(PDA)/LDA technique (Hardalupas *et al.*, 1989). A PDA is able to determine the particle diameter by comparing the phase difference from signals obtained from different photodetectors.

1.5.2 Isokinetic Sampling

The solid phase mass flux data presented above were obtained by the isokinetic sampling method which, unlike the LDA method, is intrusive. A probe is inserted into the flow and particles are extracted at a rate equal to the local flow velocity (hence, isokinetically) for a set time interval. One way to obtain isokinetic sampling is to adjust the extraction rate so that the measured pressure difference between the free stream and within the probe is negligible (Crowe *et al.*, 1998). Extracted particles are subsequently collected and weighed to give the solid phase mass per unit time, per probe cross sectional area, A_p (kg/m^{2}s). Laats (1966) and Laats and Frishman (1970) used a similar method to this to obtain mass flux data. Their gas phase measurements were also additionally obtained by attaching a rotameter to their rig which measured the suction velocity (Ivanov, Laats & Frishman, 1970).

1.5.3 Planar Imaging Measurements

Planar imaging measurements can be used to obtain the instantaneous and mean distribution of particles in a two-dimensional cross section of a two phase flow. The particle field is illuminated by a sheet of light that has usually been formed from a laser (continuous or pulsed) beam. The scattered light, as can be seen above in Figure 1.18, is proportional to the square of the particle diameter. The light is captured by a CCD camera whose number of pixels and magnification determines, in addition to the thickness of the light sheet, the spatial resolution. In the case of a pulsed laser, the pulse duration (approximately a few nanoseconds) determines the temporal

resolution, which allows the solid phase field to be essentially frozen in time.

Planar imaging measurements of the solid phase in particle-laden axisymmetric and triangular oscillating jets are to be presented below in Chapters 3 and 4, respectively. The work presented in Chapter 2 draws on previously published data of which there is a sufficient amount readily available from the literature for these purposes. However, measurements of particle distributions in axisymmetric jet flows for mass loadings in the two-way coupling regime (section 1.2.1) are not readily available, hence they are measured. Two phase velocity and mass flux measurements in a particle-laden triangular oscillating jet flow are not available because of their inherent complexity. It has been demonstrated already that single phase measurements are sufficiently difficult (Wong, 2005). Hence, planar imaging measurements are also performed in a particle-laden triangular oscillating jet flow.

1.6 Thesis Objectives

This thesis has two primary objectives:

1. To scale the distribution of flow and particles as a function of mass loading in particle-laden axisymmetric jets by correlation of existing gas and solid phase measurements, as well as new measurements of particle distributions.

2. To determine the operating conditions for which a particle-laden oscillating jet flow is superior at spreading particle distributions to that of an equivalent precessing jet flow. Further, it is intended to determine the effect of the exit mass loading on the spread of particle distributions.

The effect of mass loading on the centreline decay and spread in a particle-laden axisymmetric jet have been discussed above. The first primary objective of this thesis is to develop scaling factors that account for the reduced

centreline decay, u_o/u_c and spreading rates, $r_{1/2}$ of a particle-laden jet compared with a single phase jet, for the range of St_o reported in the literature. As has been discussed, a complete basic scaling of gas phase centreline velocity and half width measurements in particle-laden jets has not been reported. The results of the scaling will be verified with previously published experimental data such as that of Laats (1966) shown above in Figure 1.10.

Related to the first objective is the scaling of other particle-laden jet properties such as solid phase mass flux, concentration, entrainment and mean particle-distributions. While limited data is available for the first three of those properties, practically none exists for particle distributions of ϕ_o in the two-way coupling regime. Measurements of particle-distributions using a planar imaging technique like that described in section 1.5.3 are thus presented here and assessed for scaling. Some secondary investigations into the effect of exit Stokes number and gas phase exit density on particles distributions are also considered.

A planar imaging study is performed to study the effect of a triangular oscillating jet flow on particle-distributions. It is the aim of this part to determine under what conditions the oscillating jet results in a greater spread of particles than a precessing jet flow. It also aims to assess the effect of a variation of exit mass loading on particle distributions.

1.7 Thesis Outline

In Chapter 1, the basic fluid dynamics of an axisymmetric jet have been reviewed and shown that the centreline velocity and half width are inversely and directly proportional to the axial coordinate, respectively. Measurements of the gas phase in particle-laden jets have shown that particles inhibit the decay of centreline velocity and jet spread. A method to scale the gas phase centreline velocity and half width for various ϕ_o are presented in Chapter 2. Measurements from previous authors are presented throughout that chapter

to verify the scaling. These results are then used to scale other particle-laden jet properties such as the solid phase mass flux. In Chapter 3, the scaling (and lack thereof) is applied to measurements of particle distributions for a variation in ϕ_o, St_o and the jet density ratio. In Chapter 4, new measurements of particle distributions in a particle-laden triangular oscillating jet flow are presented. These are then compared with existing measurements in a particle-laden precessing jet flow. In Chapter 5, the results of the scaling of previous data and subsequent scaling of other jet properties are summarised, along with the results of the particle-laden triangular oscillating jet flow study.

Chapter 2

Mass loading and Stokes number effects in particle-laden axisymmetric jets

2.1 Introduction

Particle-laden (two-phase) turbulent axisymmetric jets have been the subject of research for more than 50 years because they have a large number of practical applications, particularly in the combustion of solid fuels. An understanding of the behaviour of particle-laden jets is necessary for the reliable modelling and optimisation of pulverised fuel burners because the interactions between the gas and the particles strongly influences heat transfer and pollutant emissions. Particle distributions are also important in many natural processes such as pollutant dispersion and the formation of rain. However, despite the significant advances in understanding, basic scaling properties of particle-laden jets are yet be reported. This task is addressed in this chapter.

In this chapter, a review of previously published data is conducted initially

to draw attention to the mechanisms considered to be the most significant in particle-laden jets. Based on this review, gas phase velocity scaling regimes are able to be defined with some physical justification. The strength of the scaling of previously published data is subsequently tested with the help of correlations. Finally, the scaling of other properties, such as solid phase mass flux and entrainment is conducted.

2.2 Interphase momentum transfer and turbulence modulation in particle-laden jets

As stated in chapter 1, the reduction in gas phase centreline velocity and jet spread with increasing ϕ_o is usually attributed to a combination of mean axial interphase momentum exchange and turbulence damping (e.g. Fleckhaus *et al.*, 1987). A description of both of these mechanisms is performed in this section.

The process of mean momentum transfer between the phases in particle-laden axisymmetric jets is typically as follows. In the near field, if the particles lag the fluid within the pipe, the mean gas phase velocity will be higher than that of the solid phase, resulting in the acceleration of the solid phase by drag. Beyond this region, the particle velocity 'overshoots' that of the gas phase as a result of particle inertia. Subsequently, particles become a source of momentum responsible for reducing the axial decay of gas phase velocity, compared with that of the single phase case. The process is illustrated in Figure 2.1, as reported by Budilarto (2003). For that particular St_o, momentum transfer from the gas to the solid phase is evident for $x/D \lesssim 5$ as seen in the slight increase in solid phase centreline velocity in that region. Beyond $x/D \gtrsim 5$, evidence of momentum transfer is seen in the reduced solid phase centreline decay rate relative to the gas phase. This mechanism has been attributed at least partly to the reduction in gas phase centreline decay with respect to the single phase case, also shown in Figure 2.1 by many authors

NOTE: This figure is included on page 37 of the print copy of the thesis held in the University of Adelaide Library.

Figure 2.1: Single, gas and solid phase centreline velocity as reported by Budilarto (2003). $St_o = 24$.

(e.g. Fleckhaus *et al.*, 1987, Hardalupas *et al.*, 1989 and Sheen *et al.*, 1994).

The relative effect of mean momentum exchange on u_c and $r_{1/2}$ are a function of St_o, and hence the slip velocity, $(u - u_p)$. Equation 1.5 shows that the momentum gained by a particle from the gas phase via the drag force is proportional to $(u - u_p)$ in the Stokes flow regime. To illustrate the effect of St_o on the slip velocity, the data of Budilarto (2003), Hardalupas *et al.* (1989) and Shuen *et al.* (1983), each with an increasing St_o, are reproduced below. These cases are thought to be representative of other data at a similar St_o. Since St_o is not constant with x/D, the mean Stokes number, St_m is introduced following Hardalupas *et al.* (1989). The critical location where $St_m \approx 1$ indicates the axial location where particles will become responsive to the decay of centreline velocity. The deceleration time scale, T_{dec} accounts for the centreline decay of gas phase velocity, defined as

$$T_{dec} = \left[\frac{du_c}{dx}\right]^{-1}. \tag{2.1}$$

The solution for this is obtained by first differentiating u_c with respect to x

(equation 1.48), which gives

$$T_{dec} = K_1 \left(\frac{D}{u_o}\right) \left(\frac{x}{D}\right)^2. \tag{2.2}$$

The ratio of the particle time scale, τ_p to T_{dec} is the mean Stokes number, where

$$St_m = \frac{\tau_p}{T_{dec}} = \frac{1}{K_1} St_o \left(\frac{D}{x}\right)^2 \tag{2.3}$$

and $K_1 \approx 0.15$ for a single phase jet.

Figure 2.2 presents the single phase, gas and solid phase centreline velocities as reported by Budilarto (2003), as well as St_m calculated according to equation 2.3 based on $St_o = 3$. These measurements correspond similarly to those of Modarress *et al.* (1984a). With increasing distance downstream from the end of the potential core, the particles move increasingly into the regime $St_m < \mathrm{O}(1)$. It is evident that particles follow closely the mean flow in the reported axial range sufficiently well. It is hypothesised therefore that since $(u - u_p) \sim 0$, then axial mean momentum transfer is small for low Stokes numbers such as that displayed in Figure 2.2. However, the rate of centreline decay and hence spread of the gas phase, is much lower for the case with particles. This may be explained by damping or attenuation of the intensity of large scale eddies by the presence of the particles.

In two phase turbulent flows, it is well known that particles may either enhance or attenuate the level of turbulence, i.e. turbulence modulation (e.g. Gore and Crowe, 1989). Gore and Crowe (1989) have inspected measured turbulence intensities in jet and pipe studies published prior to 1989. They defined the change in turbulence intensity (CTI) that occurs with the addition of particles as

$$CTI = \frac{\sigma_{tp} - \sigma_{sp}}{\sigma_{sp}}, \tag{2.4}$$

where σ_{tp} and σ_{sp} are the two and single phase turbulence intensities ($\sqrt{\overline{u'^2}}/u_c$), respectively. Gore and Crowe were able to demarcate turbulence measurements in two phase pipes and jets by the parameter d_p/l_e, where the critical

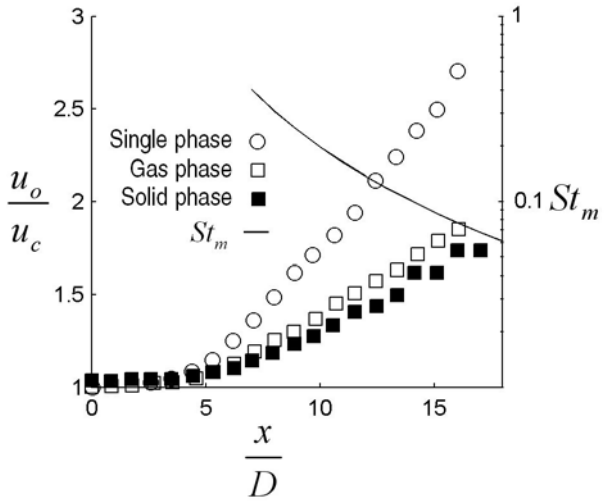

Figure 2.2: Single phase, gas phase and solid phase centreline velocity data as reported by Budilarto (2003) for $d_p = 25\mu$m, $\phi_o = 0.5$ and St_m calculated from equation 2.3. $St_o = 3$.

value of d_p/l_e is approximately 0.1, above which the sign of CTI is positive and below this it is negative, corresponding to the generation and attenuation of turbulence, respectively. It is noted however that turbulence modulation is not yet well understood and is the subject of much current research (Crowe, 2006).

Nevertheless, Gore and Crowe (1989) reasoned that, if particles are at least partially responsive to turbulent fluctuations, particles will obtain kinetic energy at the expense of the gas phase. For example, Owen (1969) showed that the average rate of work done by an eddy on N particles is equal to $3\pi\mu d_p u'^2 N\tau_p/\tau_f$. This illustrates that, for particles sufficiently responsive such that they are completely entrained into an eddy for the course of the eddy lifetime, the eddy will expend work accelerating the rms particle velocity $u'_p \rightarrow u'$ for a period equal to the particle timescale. In a turbulent jet, this could be expected to result in less energy available for large scale eddies to interact with the ambient fluid. Consequently, jet spread is impeded and hence, the decay of the centreline velocity will be reduced with increasing number of particles, or ϕ_o. For very small particles ($St << 1$),

eddies could be expected to expend minimal work on the solid phase as the particles have a quick response time. In that case, the solid phase is merely an addition to the density of the gas phase. Similarly, minimal work is lost by eddies to very large particles ($St >> 1$) since they remain in an eddy for only a brief period of time. Instead, larger particles may generate fine scale turbulence by the mechanism of vortex shedding provided $\mathrm{Re}_p > 400$ (Hetsroni, 1989). For example, Cui *et al.* (2006) assessed the dependence of CTI on St_o. They showed that the sign of CTI switches from negative to positive at approximately $St_o = 150$ (Figure 2.3). Flow visualisation also indicated that for $St_o < 150$, vortex growth is impeded, whilst for $St_o > 150$, vortex growth is enhanced Cui *et al.* (2006).

Figure 2.4 presents the single phase, gas and solid phase centreline velocities as reported by Hardalupas *et al.* (1989), as well as St_m calculated according to equation 2.3 based on $St_o = 51$. The critical value, $St_m = 1$, occurs at $x/D \approx 20$. These measurements are representative of other cases of similar St_o, such as those by Hishida *et al.* (1987) and Budilarto (2003) (Figure 2.1). The greater St_o in this figure compared with Figure 2.2, explains why a significant slip velocity develops in the near field. For $x/D < 15$, the solid phase centreline velocity is approximately constant while the gas phase decays by approximately half. Beyond that range, the solid phase decay rate approaches that of the gas phase as $x/D \rightarrow 30$. Since $(u - u_p) \neq 0$, the effects of mean momentum exchange on the gas phase decay rate are significant. Hardalupas *et al.* (1989) deduced the reduction in mean gas phase centreline decay in this data to be proportional to the momentum transferred from the solid phase, because the decay rate of mean solid phase velocity is independent of mass loading (see the closed symbols in Figure 2.4).

Figure 2.5(a) presents the single phase, gas and solid phase centreline velocities as reported by Shuen *et al.* (1983), as well as St_m calculated according to equation 2.3, based on $St_o = 799$. Also included for reference is the case $St_o = 264$, $\phi_o = 0.66$. The decay of gas phase centreline velocity for the case $St_o = 799$ is less than the case $St_o = 264$, even though ϕ_o is the same for both St_o. It is hypothesised that the reason for this can be found from

NOTE: This figure is included on page 41 of the print copy of the thesis held in the University of Adelaide Library.

Figure 2.3: *CTI* plotted versus St_o as reported by Cui et al. (2006).

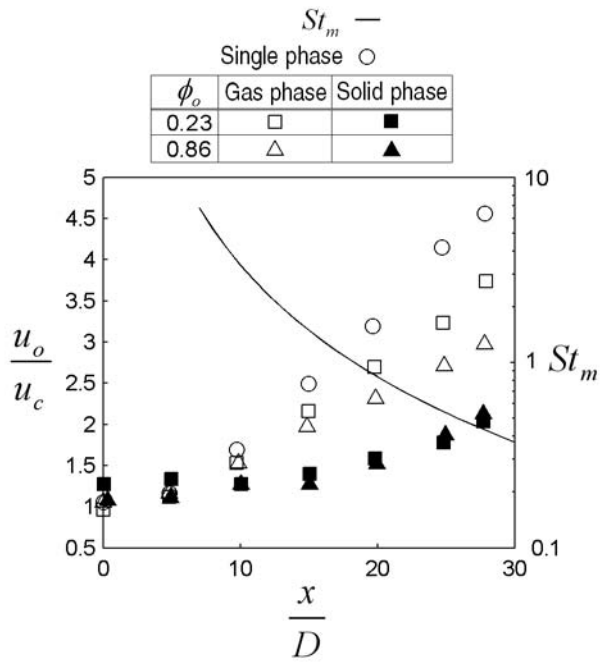

Figure 2.4: Single phase, gas phase and solid phase centreline velocity data as reported by Hardalupas et al. (1989) for $Ø_o$ = 0.23, 0.86 and St_m calculated from equation 2.3 based on St_o = 51.

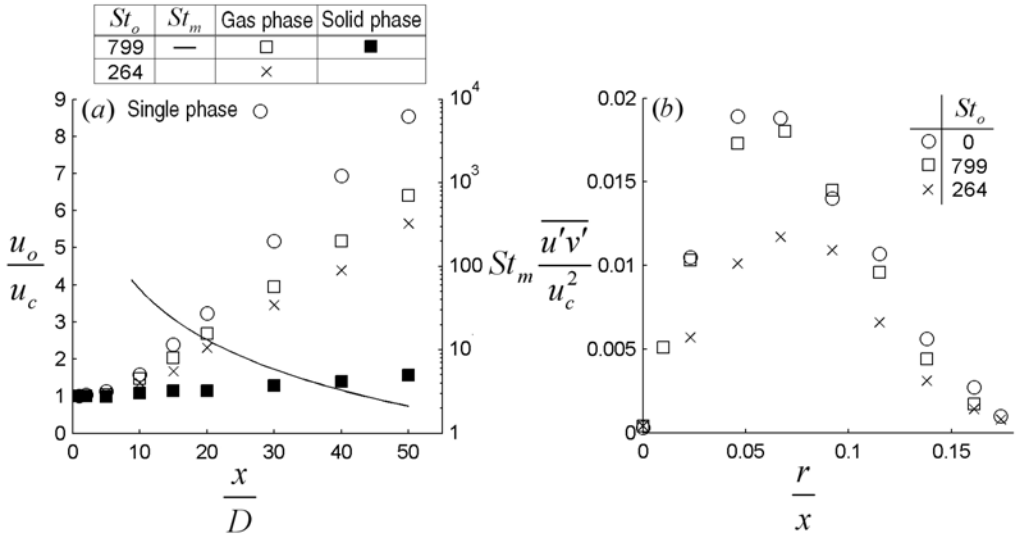

Figure 2.5: (a) Single phase, gas phase and solid phase centreline velocity data as reported by Shuen *et al.* (1988) for $\phi_o = 0.66$ and St_m calculated from equation 2.3 based on $St_o = 799$. (b) Turbulent shear stresses as reported by Shuen *et al.* (1983)

Figure 2.5(b) where the turbulent shear stress at $x/D = 20$ is reproduced for $St_o = 799$, as well as the case $St_o = 264$ for reference. Whereas the case $St_o = 264$ exhibits considerable damping of $\overline{u'v'}/u_c^2$, the turbulent stresses are essentially unmodified by the addition of the larger particles ($St_o = 799$). It is hypothesised that this can further be explained with reference to Figure 2.5(a) again. For the entire range of x/D shown, $St_m > O(1)$, meaning that the solid phase velocity is at best weakly responsive to the decay of gas phase centreline velocity over the reported axial range. As a result, it can be seen that the solid phase centreline velocity is reduced by only 50% after 50 diameters. So while there is a considerable source of solid phase momentum, the effects of turbulence damping for high Stokes numbers is small relative to the other, lower cases of St_o presented already. As suggested above already, there is likely turbulence generation of fine scale turbulence at these high Stokes numbers (Hetsroni, 1989). However, this is not expected to be a significant influence on the large scale eddies. The turbulence stress measurements as reported by Sheen *et al.* (1994) for similar St_o also only

exhibited small differences with the single phase case, despite much higher mass loadings ($\phi_o = 0.98$, 3.06).

In summary, the measurements reported by previous authors indicate that the relative effects of turbulence modulation and mean momentum exchange in particle-laden jets depend significantly on St_o. Three particular data sets, each with different magnitudes of Stokes number were presented to highlight these relative effects. These data sets are those by Budilarto (2003) for low Stokes numbers (Figure 2.2), Hardalupas *et al.* (1989) for intermediate Stokes numbers (Figure 2.4) and Shuen *et al.* (1983) (Figure 2.5) for high Stokes numbers. These measurements are representative of those reported by other authors for similar Stokes numbers. For example, the measurements of Modarress *et al.* (1984a) yield similar results for low Stokes numbers, Hishida *et al.* (1987) and Budilarto (2003) ($St_o = 24$, see Figure 2.1) for intermediate Stokes numbers and Sheen *et al.* (1994) for large Stokes numbers. Table 2.1 provides a description of the relevant details of all particle-laden jet axisymmetric pipe measurements reported in the literature for $\phi_o > 0.1$. Inspection of this data leads to the following conclusions:

- For low Stokes numbers, mean axial momentum exchange is hypothesised to be negligible, but damping of the large scale eddies is significant.

- For intermediate Stokes numbers, both mean axial momentum exchange and turbulence damping are significant.

- For larger Stokes numbers, since particles are unresponsive to large eddies, there is negligible turbulence damping but rather, particles are a significant source of axial momentum exchange.

Author	Re	D (mm)	U (m/s)	d_p (μm)	ρ_p (kg/m^3)	St_o	Fr	ϕ_o
Budilarto (2003)	8400	14.2	8.9	25	2500	3	0.79	0.25-1.0
				70		24	0.48	
Gillandt *et al.* (2001)	5700	12	7.7	110	2000	48	0.39	1.0
Fan *et al.* (1997)	53500	40	20	72	1250	10	1.19	0.22
Sheen *et al.* (1994)	20000	15	20	210	1020	186	0.87	0.98,2.75
				460		893	0.59	0.98,3.06
				780		2568	0.45	0.49-3.06
Hardalupas *et al.* (1989)	13000	15	13	80	2950	51	0.57	0.23,0.86
Tsuji *et al.* (1988)	15000	20	11	170	1020	50	0.56	2.0
	33000		24	500		950	0.64	1.85
Hishida *et al.* (1985)	22000	13	30	64	2590	76	1.47	0.3
Shuen *et al.* (1985)	22000	10.9	30	79	2620	140	0.91	0.2
	19000		25	119		264	1.69	0.2,0.66
	19000			207		799	1.32	0.66
Modarress *et al.* (1984a)	13300	20	10	50	2990	12	0.55	0.32,0.85
Modarress *et al.* (1984b)	14100	20	10	200	2990	191	0.28	0.8
Subramanian & Raman (1984)	25000	25.4	15	165	3200	160	0.4	0-2.5
Laats & Frishman (1970)	120000	35	50	17	3950	5	3.31	0.3
				32		18	2.27	0.3-1.4
				49		42	1.83	0.3,0.4
				72		91	1.44	0.3
Laats (1966)	74000	27	40	40	2550	19	2.14	0.2-1.0

Table 2.1: The experimental conditions under which previous particle-laden pipe jet investigations were conducted where d_p is based mostly on the volume or mass averaged diameter except for Shuen *et al.* (1985), where d_p is the Sauter mean diameter. Measurements conducted prior to 1984, excluding those of Modarress *et al.* (1984a,b) used an isokinetic sampling tube and rotameter arrangement (see section 1.5.2). Measurements conducted since 1984 used some LDA or PDA based technique (see section 1.5.1)

2.3 Power-law scaling of the gas phase

Based on the conclusions from the previous section, three different power-law scaling regimes are proposed for the data shown in Table 2.1. They are, in the order presented, the high Stokes number regime, $St_o \gtrsim 200$, the intermediate Stokes number regime, $20 \lesssim St_o \lesssim 200$ and the low Stokes number regime $St_o \lesssim 20$. These values of St_o are based on the linear correlation analysis presented below. Previously published data (see table 2.1) will be presented to verify the proposed scaling.

An assessment of the strength of each correlation of data is performed with the help of the correlation coefficient which is defined as

$$R_{xu} = \frac{\sum (x_i - \overline{x})(u_i - \overline{u})}{\sqrt{\sum (x_i - \overline{x})^2 \sum (u_i - \overline{u})^2}}, \tag{2.5}$$

where x_i represents $(x/D)(1+\phi_o)^{-n}$ values (Here, $n = 1$ or $1/2$ depending on St_o), u_i represents u_o/u_c values and the over bar denotes the mean. The half width correlation coefficient, $R_{xr_{1/2}}$ is defined similarly. Data points outside the region of linear jet growth ($x/D \lesssim 7$) are not included in correlations. The squared correlation coefficient R^2_{xu} is used to accentuate departures from $R_{xu} \approx 1$. For example, the collapse of Laats' centreline and half width in Figure 2.12(a) and (b) below, yields $R^2_{xu} = 0.996$ and $R^2_{xr_{1/2}} = 0.994$, respectively. The correlation coefficient associated with 'uncorrected' data (x_i representing x/D values alone in equation 2.5) is denoted $\underline{R}^2_{xu}$, $\underline{R}^2_{xr_{1/2}}$. For example, Laats' unscaled data yields $\underline{R}^2_{xu} = 0.69$ and $\underline{R}^2_{xr_{1/2}} = 0.54$.

2.3.1 The high Stokes number regime, $St_o \gtrsim 200$

While Melville and Bray (1979) provided an empirical exponential scaling as reproduced in Figure 1.12, they also attempted a power-law scaling. However, they attempted to apply their power-law scaling to data in the regime $St_o \lesssim$

20, which was the only available data at the time. It is contended here that their solution applies for the regime $St_o \gtrsim 200$. Recall the functions $a(\phi_o)$ and $b(\phi_o)$ defined above by equations 1.53 and 1.54. Melville and Bray's power-law scaling takes the form, $a(\phi_o) = (1+\phi_o)^{-1/2}$ and $b(\phi_o) = 1$, hence

$$\frac{u_o}{u_c} = K_1 \frac{x}{D} \left(\frac{1}{1+\phi_o} \right)^{1/2} \tag{2.6}$$

and

$$\frac{r_{1/2}}{D} = K_2 \frac{x}{D}. \tag{2.7}$$

In essence, equations 2.6 and 2.7 are equivalent to the far field solutions of a variable density jet. This is seen by the scaling of the centreline velocity by the effective jet diameter (Beer and Chigier, 1972), $D(\rho_o/\rho)^{1/2}$, where the particle-laden jet exit density, $\rho_o = \rho(1+\phi_o)$, while the jet spread is independent of ϕ_o (Chen and Rodi, 1981).

Equation 2.6 is a consequence of the complete far field transfer of momentum from the solid to the gas phase. The conservation of total (gas and solid) momentum is described by

$$\int_A \rho u^2 (1+\phi) dA = \pi \rho (1+\phi_o) u_o^2 r_o^2. \tag{2.8}$$

Here, A is the cross-sectional area of the jet and $\phi = \phi(x, r)$ is the spatial variation of mass loading. Substitution of the functions $g(\eta) = \phi/\phi_c$ and $f(\eta) = u/u_c$ gives

$$2\pi \rho u_c^2 r_{1/2}^2 \left[\int_0^\infty f^2(\eta) \eta d\eta + \phi_c \int_0^\infty g(\eta) f^2(\eta) \eta d\eta \right] = \pi \rho (1+\phi_o) u_o^2 r_o^2. \tag{2.9}$$

In the far-field, the absolute centreline mass concentration of particles, $\phi_c \to 0$, hence equation 2.9 becomes

$$2\pi \rho u_c^2 x^2 \int_0^\infty f^2(\eta) \eta d\eta \sim \pi \rho (1+\phi_o) u_o^2 r_o^2, \tag{2.10}$$

so that in the far field, practically all momentum is carried by the gas phase

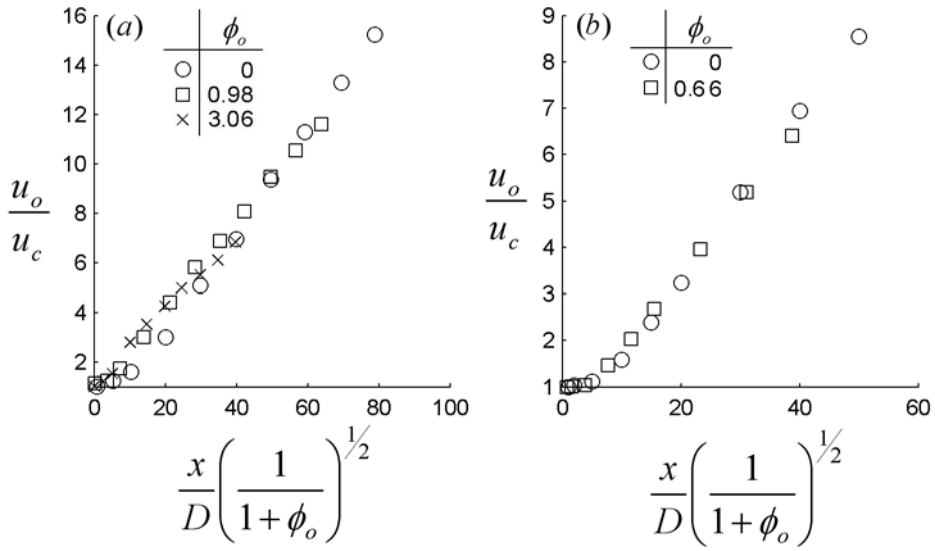

Figure 2.6: Gas phase centreline velocities as reported by (a) Sheen *et al.* (1994) ($St_o = 950$, $R^2_{xu} = 0.99$, $\underline{R}^2_{xu} = 0.72$) and (b) Shuen *et al.* (1983) ($St_o = 799$, $R^2_{xu} = 0.99$, $\underline{R}^2_{xu} = 0.88$), but plotted as functions of $x/D(1+\phi_o)^{-1/2}$.

as proposed by Melville and Bray (1979). This equation implies that $u_c \propto \frac{1}{x}(1+\phi_o)^{1/2}$, i.e. equation 2.6. It is believed that the weak dependence of $r_{1/2}$ on ϕ_o in this regime is a consequence of the unresponsive nature of very large particles to large eddies. Hence, the extraction of turbulence kinetic energy from the gas phase by the action of the particles is not significant and turbulent mixing and jet spread in a two phase jet proceeds similarly to that of a single phase jet.

Shown in Figure 2.6 are gas phase centreline velocities as reported by Sheen *et al.* (1994) (a) and Shuen *et al.* (1983) (b), but plotted as functions of $x/D(1+\phi_o)^{-1/2}$. A poor collapse of u_c in the near field in Figure 2.6(a) is evident. In contrast, the collapse of Shuen *et al.*'s measurements are good for the reported axial range. This may be related to Shuen *et al.*'s slightly lower St_o compared with Sheen *et al.*'s. This appears to be consistent with the poor collapse of u_o/u_c in the near field for very high St_o in the data of Tsuji *et al.* (1988) plotted as functions of $x/D(1+\phi_o)^{-1/2}$ in Figure 2.7(a). Since this regime is suspected to be a far-field scaling regime (as equation 2.10

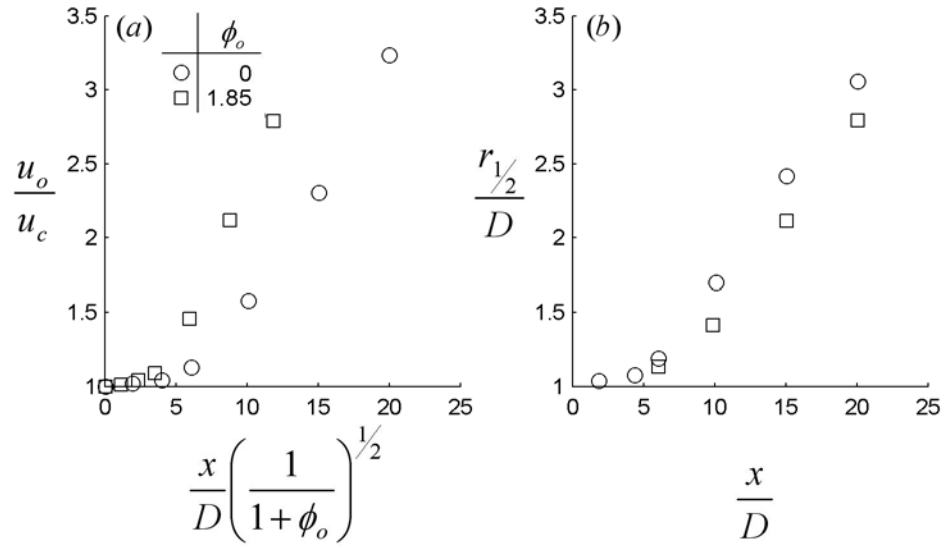

Figure 2.7: Gas phase centreline velocity plotted as a function of $x/D(1+\phi_o)^{-1/2}$ (a) and velocity half width (b) as reported by Tsuji *et al.* (1988),. $St_o = 950$, $R^2_{xu} = 0.81$, $\underline{R}^2_{xu} = 0.96$.

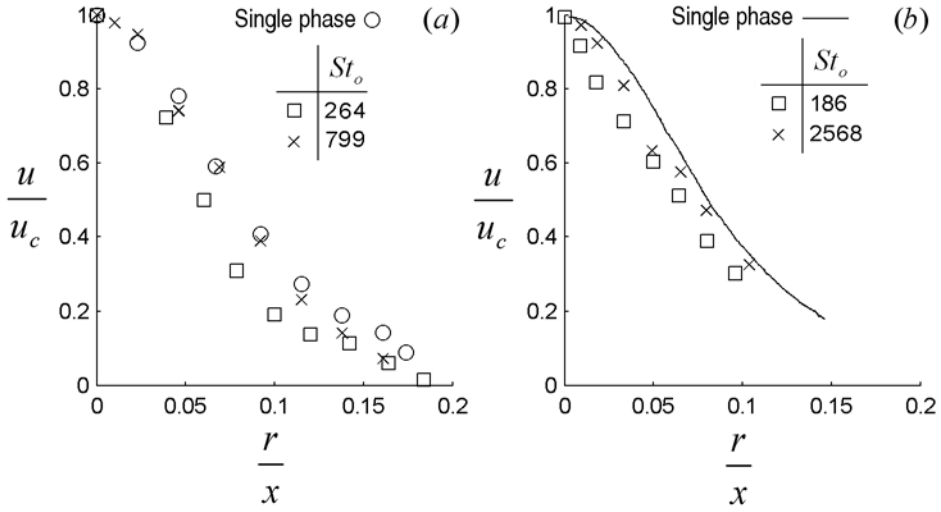

Figure 2.8: Radial velocity profiles as reported by (a) Shuen *et al.* (1983) and (b) Sheen *et al.* (1994) for $\phi_o = 0.66$, $x/D = 40$ and $\phi_o = 0.98$, $x/D = 60$, respectively.

implies), the high Stokes number data of Tsuji *et al.* (1988) is not included below in Figure 2.14. Figure 2.7(b) illustrates the weak dependence of $r_{1/2}$ on ϕ_o in Tsuji *et al*'s data. The relatively weak dependence of $r_{1/2}$ on ϕ_o can be seen further in the radial profiles of Figure 2.8, reproduced from Shuen *et al.* (1983) and Sheen *et al.* (1994). For constant ϕ_o, the comparatively lower spread for smaller St_o is evident. To this author's knowledge, there is no available data of half widths published for the very far field in this regime, thus, equation 2.7 can not be fully assessed.

2.3.2 The intermediate Stokes number regime, $20 \lesssim St_o \lesssim 200$

In this regime it is hypothesised that $a(\phi_o) = (1 + \phi_o)^{-1}$ and $b(\phi_o) = (1 + \phi_o)^{-1/2}$, hence

$$\frac{u_o}{u_c} = K_1 \frac{x}{D} \left(\frac{1}{1 + \phi_o} \right) \tag{2.11}$$

and

$$\frac{r_{1/2}}{D} = K_2 \frac{x}{D} \left(\frac{1}{1 + \phi_o} \right)^{1/2}. \tag{2.12}$$

These equations are consistent, as with the previous regime, with the complete far-field transfer of momentum from the solid to the gas phase. In equation 2.9, the similarity variable $\eta = r/x$ was used under the assumption that the half widths were independent of x. In this regime, $\xi = r/r_{1/2}$ is the chosen similarity parameter because it accounts for the dependence of $r_{1/2}$ on ϕ_o in gas phase velocity radial profiles (see Laats and Frishman, 1970). If profiles were normalised by $\eta = r/x$ in this regime, they would not be self-similar as they become narrower with increasing x/D as described by equation 2.12. Substituting the functions $g(\xi) = \phi/\phi_c$ and f into equation 2.8 gives

$$2\pi\rho u_c^2 r_{1/2}^2 \left[\int_0^\infty f^2(\xi)\xi d\xi + \phi_c \int_0^\infty g(\xi) f^2(\xi)\xi d\xi \right] = \pi\rho(1 + \phi_o) u_o^2 r_o^2. \tag{2.13}$$

Similarly to above, it is inevitable that the absolute centreline mass loading will approach zero with increasing x, i.e $\phi_c \to 0$ as $x \to \infty$. Hence, equation 2.13 becomes

$$2\pi\rho u_c^2 r_{1/2}^2 \int_0^\infty f^2(\xi)\xi d\xi \approx \pi\rho(1+\phi_o)u_o^2 r_o^2, \tag{2.14}$$

and thus

$$r_{1/2} \propto \frac{(1+\phi_o)^{1/2}}{u_c}. \tag{2.15}$$

The increased dependence of $r_{1/2}$ on ϕ_o in this regime compared with that for $St_o \gtrsim 200$, is a consequence of the increase in turbulence damping. For high Stokes numbers, the extraction of turbulent kinetic energy from the gas phase by the particles is negligible since the particles are effectively unresponsive. For intermediate Stokes numbers, particles exhibit a partial response to large eddies and hence kinetic energy is obtained by the particles at the expense of the gas phase. Consequently, there is a damping of the large eddies, those most responsible for entrainment of the ambient fluid. The damping is expected to occur mostly in the near field since the concentration of particles rapidly approaches zero as described by equation 2.14.

Shown in Figure 2.9 are gas phase centreline velocities as reported by Shuen *et al.* (1985) and Tsuji *et al.* (1988) plotted as functions of $x/D(1+\phi_o)^{-1}$. In Figure 2.10 are half widths as reported by Laats and Frishman (1970) and Hishida *et al.* (1985), but plotted as functions of $x/D(1+\phi_o)^{-1/2}$. The centreline velocity measurements of Budilarto (2003) and Hardalupas *et al.* (1989), but plotted as functions of $x/D(1+\phi_o)^{-1}$, indicate that for their data, the correlations get progressively worse as ϕ_o is increased (see Figure 2.11). The effect of larger ϕ_o on the scaling of half widths can not be assessed since, to this author's knowledge, half widths for loadings greater than 0.3 have not been published.

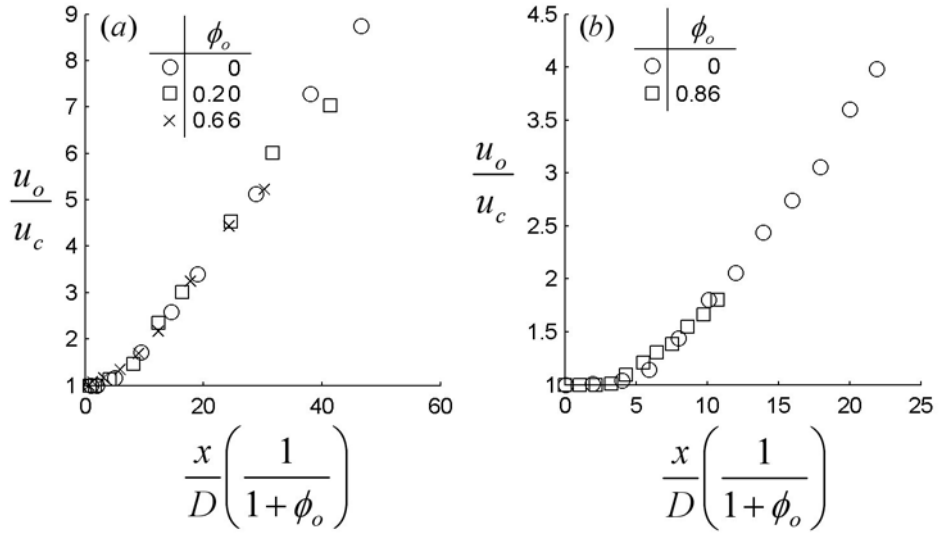

Figure 2.9: Gas phase centreline velocity as reported by (a) Shuen *et al.* (1985) ($St_o = 264$, $R^2_{xu} = 0.99$, $\underline{R}^2_{xu} = 0.88$) and by (b) Tsuji *et al.* (1988) ($St_o = 50$, $R^2_{xu} = 0.98$, $\underline{R}^2_{xu} = 0.58$), but plotted as functions of $x/D(1+\phi_o)^{-1}$.

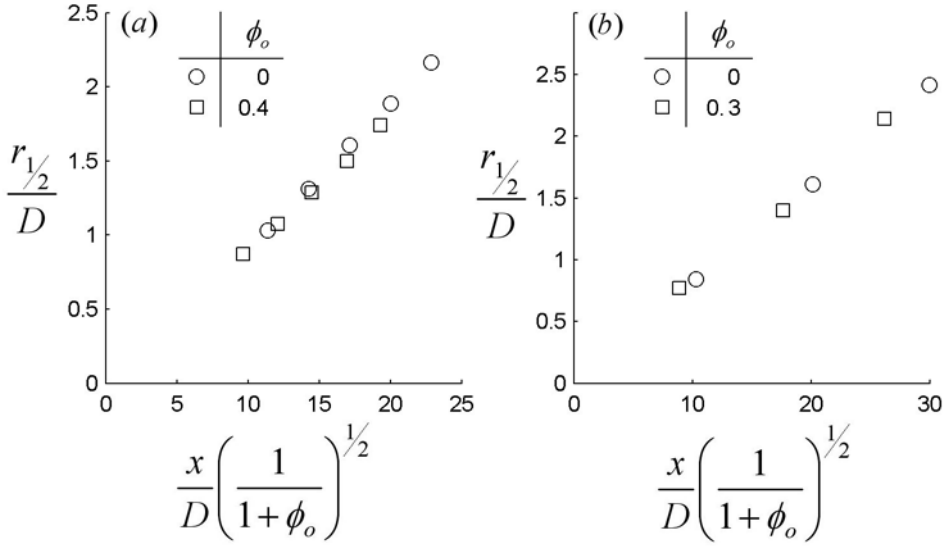

Figure 2.10: Gas phase velocity half widths as reported by (a) Laats and Frishman (1970) ($St_o = 42$, $R^2_{xr_{1/2}} = 0.99$, $\underline{R}^2_{xr_{1/2}} = 0.82$) and by (b) Hishida *et al.* (1985) ($St_o = 76$, $R^2_{xr_{1/2}} = 0.99$, $\underline{R}^2_{xr_{1/2}} = 0.97$), but scaled according to equation 2.12.

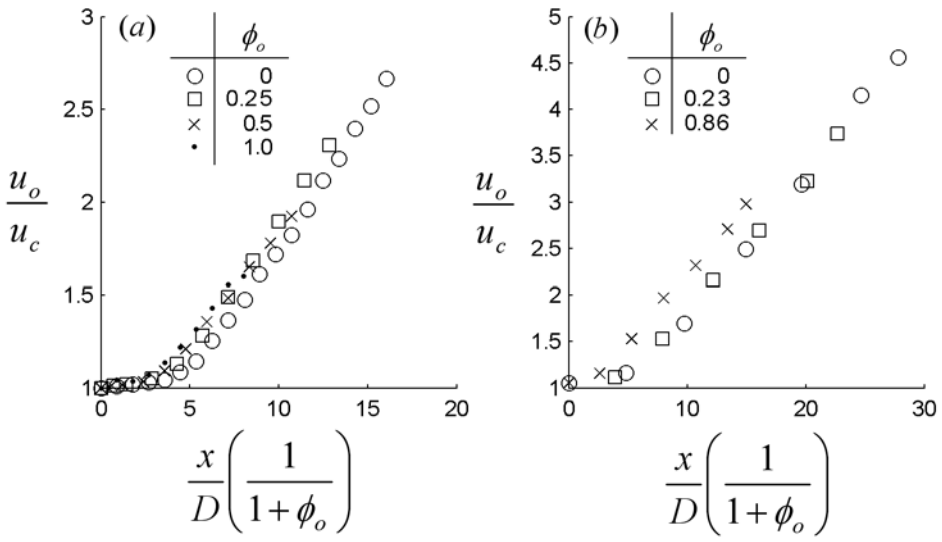

Figure 2.11: Gas phase centreline velocity half widths as reported by (a) Budilarto (2003) ($St_o = 24$, $R^2_{xr_{1/2}} = 0.97$, $\underline{R}^2_{xr_{1/2}} = 0.58$) and by (b) Hardalupas *et al.* (1989) ($St_o = 51$, $R^2_{xr_{1/2}} = 0.95$, $\underline{R}^2_{xr_{1/2}} = 0.76$), but scaled according to equation 2.12.

2.3.3 The low Stokes number regime, $St_o \lesssim 20$

In this regime, it is hypothesised that $a(\phi_o) = (1 + \phi_o)^{-1}$ and $b(\phi_o) = (1 + \phi_o)^{-1}$, hence

$$\frac{u_o}{u_c} = K_1 \frac{x}{D} \left(\frac{1}{1 + \phi_o} \right), \tag{2.16}$$

and

$$\frac{r_{1/2}}{D} = K_2 \frac{x}{D} \left(\frac{1}{1 + \phi_o} \right). \tag{2.17}$$

These equations are consistent with the negligible transfer of momentum from the solid to the gas phase. If a jet is laden with particles fine enough that they are able to respond sufficiently well to large scale turbulent motions, then it can be assumed to a first-order approximation, that the time averaged axial velocity of both phases are almost equal, i.e. $u \approx u_p$. For example, the measurements of Budilarto (2003) show that the axial component of the solid phase velocity is within approximately 10% of the gas phase velocity

for $x/D < 20$, $St_o = 3$ and $\phi_o = 0.5$ (Recall Figure 2.1). Consequently, in this low St_o regime, the effects of mean interphase momentum exchange are expected to be small.

The relationship between the centreline velocity, u_c, and $r_{1/2}$ is found from the conservation of mean gas phase momentum,

$$\frac{d}{dx} 2\pi\rho \int_0^\infty u^2 r dr \approx 0, \tag{2.18}$$

where the contribution of the solid phase momentum has been neglected, consistent with there being negligible mean momentum transfer between the phases (i.e. $u \approx u_p$). If the slip velocity is small, there is no significant exchange of mean axial momentum between the phases. Substitution of f into this equation gives $u_c \propto 1/r_{1/2}$ (see equation 1.46), consistent with equations 2.16 and 2.17. It should also be noted that Melville and Bray's exponential scaling applied to data in this regime (Figure 1.12) is also consistent with equation 2.18. In this regime, the stronger dependence of $r_{1/2}$ on ϕ_o compared with the other regimes is a result of the much stronger damping of the large eddies since particles are assumed 'responsive' to turbulent fluctuations. Hence, responsive particles obtain a greater portion of kinetic energy at the expense of the gas phase compared with partially responsive particles. Figures 2.12 and 2.13 show that the gas phase centreline velocity and half width measurements of Laats (1966), Modarress *et al.* (1984a) and Laats and Frishman (1970), for $St_o = 19$, 12 and 18, respectively, collapse if plotted as functions of $x/D(1 + \phi_o)^{-1}$.

2.3.4 Summary of correlations

The power-law scaling of the gas phase centreline velocity and half-width for three regimes of exit Stokes number are summarised in Figure 2.14. Not included are measurements that are judged to have not been carried out far enough downstream to provide a reliable or strong linear correlation (Mostafa

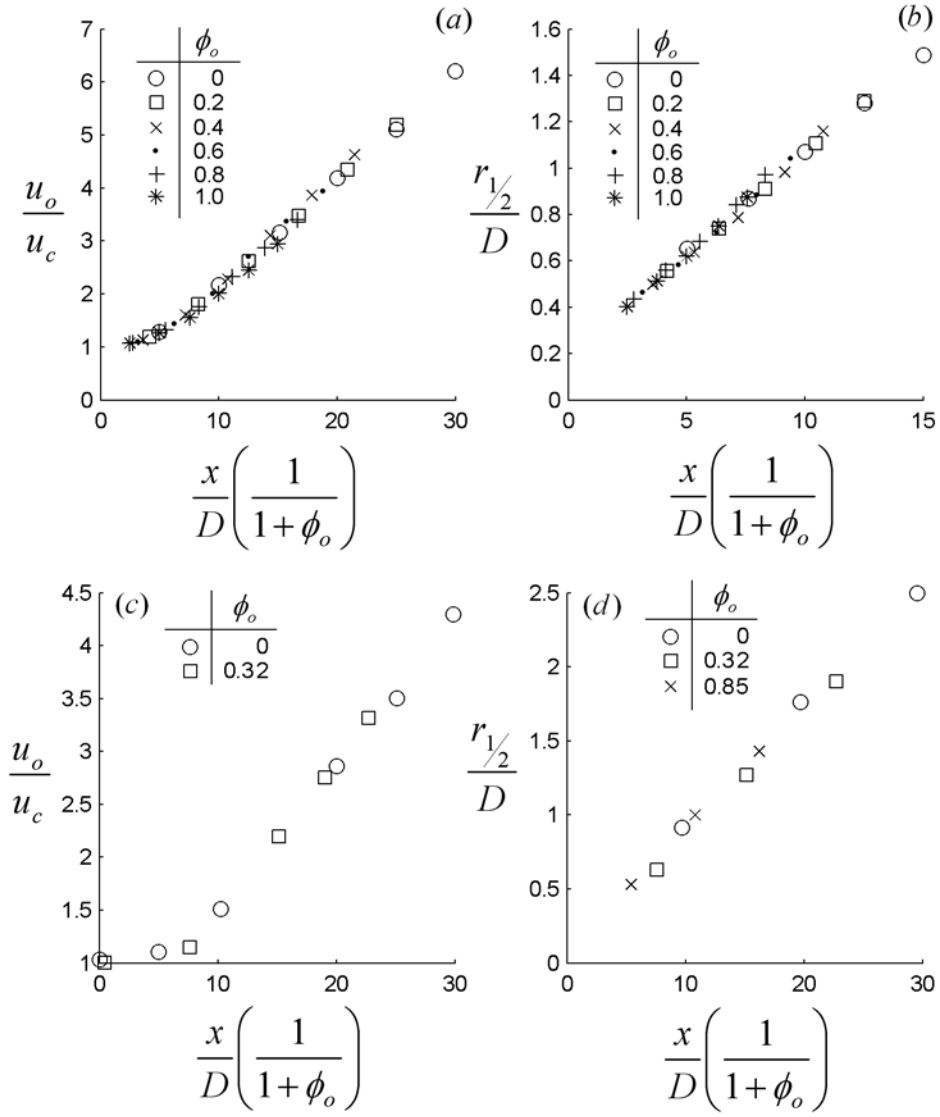

Figure 2.12: Gas phase centreline velocity as reported by (a) Laats (1966) (St_o = 19, R^2_{xu} = 0.99, $\underline{R}^2_{xu}$ = 0.69) and (c) Modarress *et al.* (1984a) (St_o = 12, R^2_{xu} = 0.99, $\underline{R}^2_{xu}$ = 0.86), plotted as functions of $x/D(1+\phi_o)^{-1}$. Half widths as reported by (b) Laats (1966) ($R^2_{xr_{1/2}}$ = 0.99, $\underline{R}^2_{xr_{1/2}}$ = 0.54) and (d) Modarress *et al.* (1984a) ($R^2_{xr_{1/2}}$ = 0.99, $\underline{R}^2_{xr_{1/2}}$ = 0.69), plotted as functions of $x/D(1+\phi_o)^{-1}$.

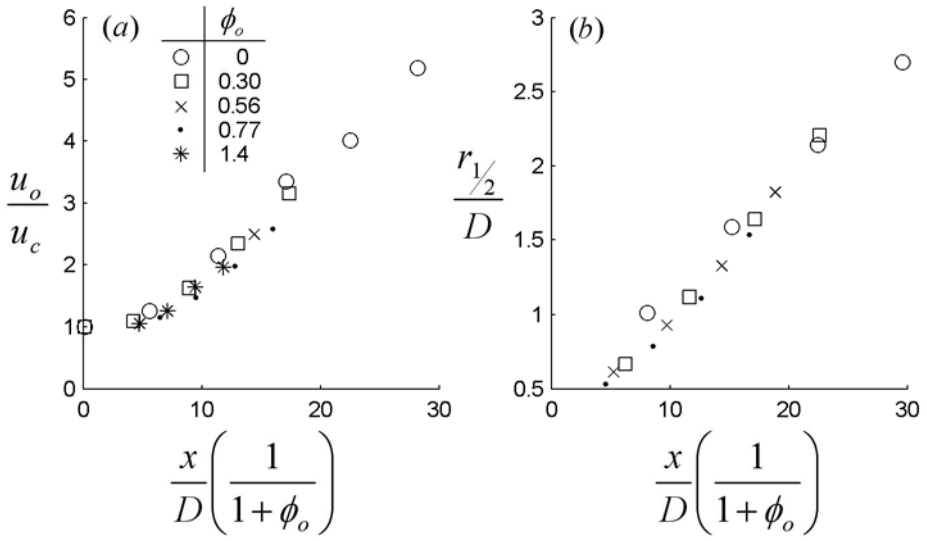

Figure 2.13: Gas phase centreline velocity and half width as reported by Laats and Frishman (1970) plotted as functions of $x/D(1+\phi_o)^{-1}$. $St_o = 18$, $R^2_{xu} = 0.98$, $R^2_{xr_{1/2}} = 0.99$, $\underline{R}^2_{xu} = 0.31$ and $\underline{R}^2_{xr_{1/2}} = 0.52$.

et al., 1989, Tsuji *et al.*, 1988, for the cases other than $St_o = 50$) and flows issuing from smooth contractions (Ferrand *et al.*, 2001). Circles and squares denote data that has been scaled with $x/D(1+\phi_o)^{-1}$ and $x/D(1+\phi_o)^{-1/2}$, respectively. Note that a circle overlaid with a square indicate Fan *et al.*'s (1997) measurements which scale with both $x/D(1+\phi_o)^{-1}$ ($\phi_o = 0.22$) and $x/D(1+\phi_o)^{-1/2}$ ($\phi_o = 0.8$) depending on the loading (see Figure 2.16 below) for $St_o = 10$.

The approximate critical values between circles and squares was used to estimate the critical values of St_o. For $St_o \lesssim 200$, u_o/u_c scales with $x/D(1+\phi_o)^{-1}$, and within that range, $r_{1/2}$ scales with $x/D(1+\phi_o)^{-1/2}$ for $20 \lesssim St_o \lesssim 200$. Beyond $St_o \approx 200$, u_o/u_c scales with $x/D(1+\phi_o)^{-1/2}$. However, the value of 200 is an order of magnitude estimate since some centreline velocity data scales with $x/D(1+\phi_o)^{-1/2}$ for $St_o < 200$ (Gillandt *et al.*, 2001), and some with $x/D(1+\phi_o)^{-1}$ for $St_o > 200$ (Shuen *et al.*, 1985).

These inconsistencies, as well as anomalies presented in the next section,

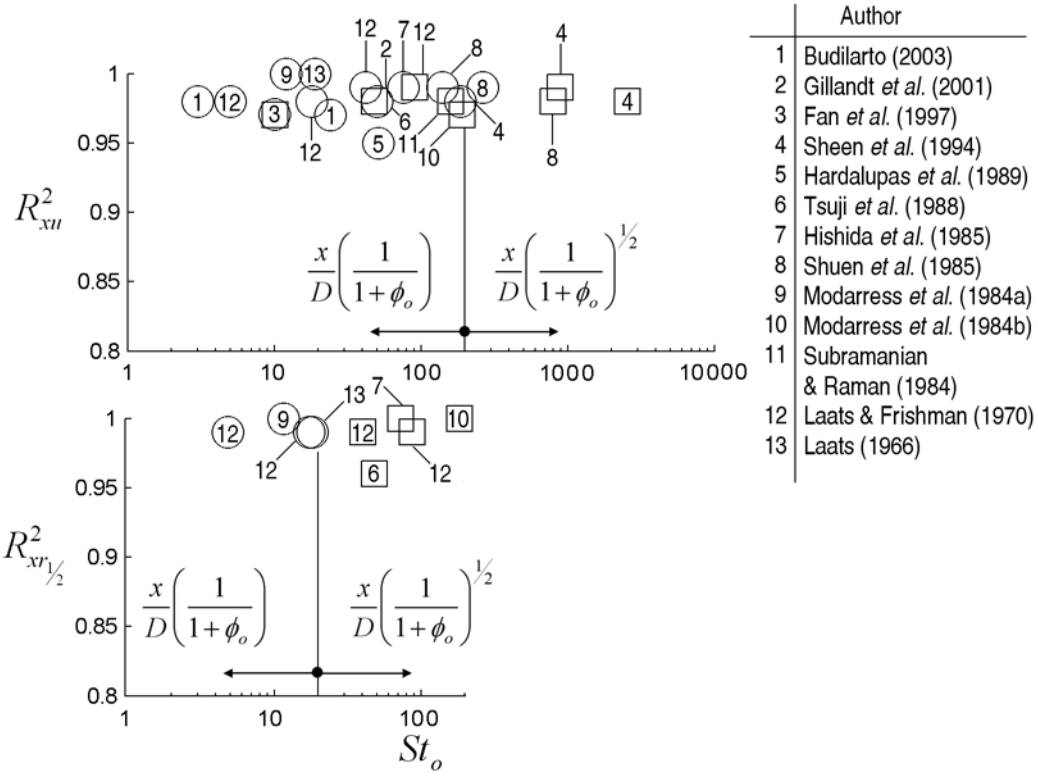

Figure 2.14: Results of the linear correlation analysis of scaled gas phase centreline velocities and half widths using previously published data. Circles and squares denote data that scaled with $x/D(1+\phi_o)^{-1}$ and $x/D(1+\phi_o)^{-1/2}$, respectively. Vertical lines and horizontal arrows indicate the approximate critical values.

are expected to be partly due to the complicating influence of gravity, the importance of which may be assessed with the help of the particle Froude number, defined as

$$Fr^2 = \frac{\rho}{\rho_p}\frac{u^{*2}}{gd_p}, \tag{2.19}$$

where u^* is the friction velocity (see equation 3.2 below). Gravity is of small importance for $Fr > 1$ (Liljegren and Vlachos, 1990). From Table 2.1, it can be seen that the ambiguous data as suggested in the paragraph above and in the next section, has a Froude number well below 1 (e.g. Gillandt *et al.*, 2001, $Fr = 0.39$). Hence, a complete mathematical description of these scaling regimes would have to take into account the effects of gravity. Also, in practice, the particle size distribution is rarely fully monodisperse so that a range of St_o is present in each flow. This is also expected to contribute to the ambiguity of the exact regime boundaries. See Table 2.1 for details of the experimental conditions for data used in Figure 2.14.

The numerical values of R^2_{xu} and $R^2_{xr_{1/2}}$ as illustrated in Figure 2.14 are listed in Table 2.2. Also included for reference are unscaled correlation coefficients, i.e. $\underline{R}^2_{xu}$ and $\underline{R}^2_{xr_{1/2}}$. In addition, values of R^2_{xu} and $R^2_{xr_{1/2}}$ are provided for different exponents, i.e. $n = 1$ and $1/2$. The exponent $n = 1/3$ is also included to detect the sensitivity of R^2_{xu} and $R^2_{xr_{1/2}}$ for a variation in the exponent. Highlighted in bold are the proposed scaling regime for each data set. It can be seen that $\underline{R}^2_{xu}$ is often comparatively high (e.g. Hishida *et al.*, 1985, $\underline{R}^2_{xu} = 0.94$) due to a comparatively low mass loading (e.g. $\phi_o = 0.3$), hence the centreline velocity differs minimally from the single phase case. Hence sometimes, the exact scaling regime is ambiguous. However, for a high variation in mass loading (e.g. Sheen *et al.*, 1994, $\phi_o = 0 - 2.75$, $St_o = 186$), $\underline{R}^2_{xu} = 0.41$ is comparatively low, and hence, $R^2_{xu} = 0.98$ (exponent, $n = 1$) is unambiguous. As the exponent is reduced from 1 to 1/2 and 1/3, R^2_{xu} is reduced to values of 0.89 and 0.78 respectively, thus illustrating the lower correlation for the coefficients of $n = 1/2$ and $1/3$ in this particular case. Some departure occurs for some cases, however. For example, Sheen *et al.* (1994), $St_o = 893$ gives $R^2_{xu}(n = 1/2) = 0.99$, while only a relatively small

		Power-law Exponent, n							
		0		1		1/2		1/3	
Author	St_o	$\underline{R}^2_{xu}$	$\underline{R}^2_{xr_{1/2}}$	R^2_{xu}	$R^2_{xr_{1/2}}$	R^2_{xu}	$R^2_{xr_{1/2}}$	R^2_{xu}	$R^2_{xr_{1/2}}$
Budilarto (2003)	3	0.56	-	**0.99**	-	0.86	-	0.82	-
	24	0.60	-	**0.97**	-	0.86	-	0.79	-
Gillandt *et al.* (2001)	48	0.76	-	0.92	-	**0.98**	-	0.92	-
Fan *et al.* (1997)	10	0.80	-	**0.97**	-	0.90	-	0.76	-
Sheen *et al.* (1994)	186	0.41	-	**0.98**	-	0.89	-	0.78	-
	893	0.72	-	0.89	-	**0.99**	-	0.96	-
	2568	0.84	-	0.83	-	**0.98**	-	0.99	-
Hardalupas *et al.* (1989)	51	0.76	-	**0.95**	-	0.96	-	0.92	-
Tsuji *et al.* (1988)	50	0.52	0.46	**0.98**	0.92	0.90	**0.96**	0.81	0.90
	950	0.95	0.94	0.43	0.45	0.81	0.83	0.86	0.88
Hishida *et al.* (1985)	76	0.94	0.97	**0.99**	0.97	0.99	**0.99**	0.98	0.99
Shuen *et al.* (1985)	140	0.98	-	**0.99**	-	0.99	-	0.98	-
	264	0.80	-	**0.99**	-	0.86	-	0.84	-
	799	0.85	-	0.98	-	**0.98**	-	0.95	-
Modarress *et al.* (1984a)	12	0.70	0.86	**0.99**	**0.99**	0.97	0.93	0.94	0.87
Modarress *et al.* (1984b)	191	0.95	0.91	0.80	0.89	**0.97**	**0.99**	0.99	0.99
Subramanian & Raman (1984)	160	0.40	-	0.91	-	**0.98**	-	0.83	-
Laats & Frishman (1970)	5	0.67	0.71	**0.98**	**0.98**	0.95	0.89	0.88	0.84
	18	0.31	0.69	**0.98**	**0.98**	0.80	0.90	0.66	0.84
	42	0.89	0.83	**0.98**	0.89	0.98	**0.99**	0.96	0.98
	91	0.96	0.94	0.94	0.96	**0.99**	**0.99**	0.99	0.97
Laats (1966)	19	0.69	0.68	**0.99**	**0.99**	0.94	0.93	0.87	0.87

Table 2.2: Numerical values of squared correlation coefficients R^2_{xu} and $R^2_{xr_{1/2}}$ of scaled and unscaled data for power-law exponents of 0 (unscaled data), 1, 1/2 and 1/3.

reduction in $R^2_{xu}(n = 1/3) = 0.96$ is detected. For two data sets, it was found that $R^2_{xu}(n = 1/3)$ is greater than $R^2_{xu}(n = 1/2)$ (Sheen *et al.*, 1994, $St_o = 2568$ and Modarress *et al.*, 1984b, $St_o = 191$). Since these two data sets have very low Froude numbers, gravity, as discussed above, is expected to be significant (see Table 2.1 for values of Fr for each case).

2.3.5 Anomalous Results

This section reviews data that doesn't fit well into any of the regimes described above. Some anomalous results can be expected due to the wide range of experimental conditions and measurement techniques. This is not to suggest that there is anything necessarily wrong with such data, but rather, the simplicity of the scaling proposed above does not account fully for what is a complex interaction of flow and particles. Some measurements (i.e. Ferrand

et al., 2001 and Wall *et al.*, 1982) in axisymmetric jets with slightly different boundary conditions, i.e. a smooth contraction orifice, are also considered here.

Modarress *et al.* (1984b) find a clear dependence of $r_{1/2}$ on ϕ_o, where $r_{1/2}$ may scale according to equation 2.12 (Figure 2.15b). However, in contrast to the scaled data presented in section 2.3.2, the centreline scales with $x/D(1+\phi_o)^{-1/2}$ (see Figure 2.15a). This may be related to that fact that the Stokes number of this data ($St_o = 191$) is straddling the proposed regime boundaries (see Figure 2.14), i.e. $St_o \approx 200$.

The gas phase centreline velocities as reported by Fan *et al.* (1997) contradict the assumption that the scaling regime is a function of St_o only (see Figure 2.14). They found that the centreline velocity for the case $\phi_o = 0.22$ scales with $x/D(1+\phi_o)^{-1}$ while the case $\phi_o = 0.8$ scales with $x/D(1+\phi_o)^{-1/2}$, for a constant $St_o = 10$ (Figure 2.16). Based on this Stokes number, this data is in the regime where scaling with $x/D(1+\phi_o)^{-1}$ would be expected (see Figure 2.14).

Whereas all data presented above were obtained from particle-laden jets issuing from a pipe (Table 2.1), measurements conducted by Ferrand *et al.* (2001) and Wall *et al.* (1982) were conducted for a jet issuing from a smooth contraction. In addition, the droplet-size distribution of Ferrand *et al.* (2001) is polydisperse with a range of diameters from 1-90μm. The mass averaged diameter is $d_p = 60\mu$m (Ferrand *et al.*, 2003). Despite these complications, Ferrand *et al.*'s gas phase centreline velocity measurements scale with $x/D(1+\phi_o)^{-1}$ satisfactorily (Figure 2.17b). Wall *et al.* (1982) reported spreading coefficients, K_2 for a range of St_o, which collapse if scaled with $x/D(1+\phi_o)^{-1/2}$ (Figure 2.17b), for constant St_o. These results suggests that the critical values may depend on the boundary conditions.

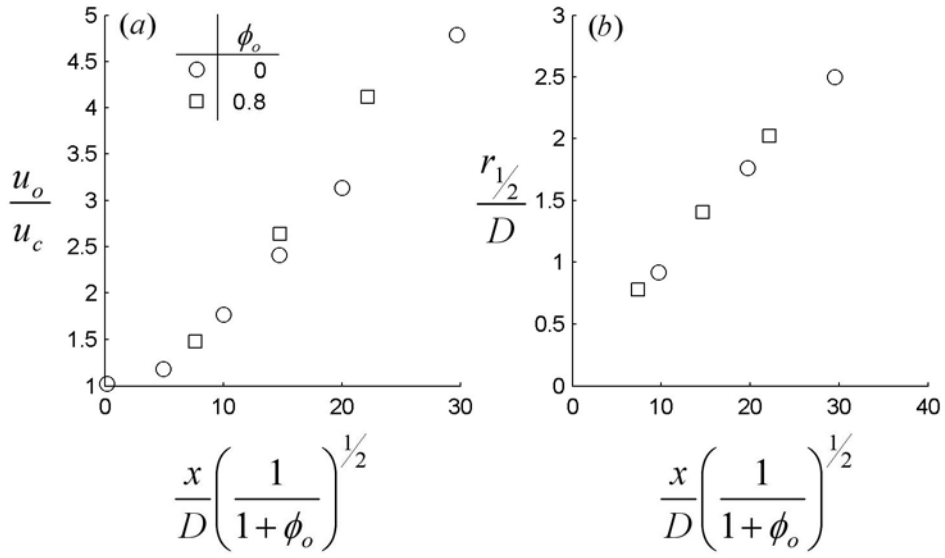

Figure 2.15: Gas phase centreline velocity (a) and velocity half width (b) as reported by Modarress *et al.* (1984b), but scaled according to equations 2.6 and 2.7, respectively. $St_o = 191$.

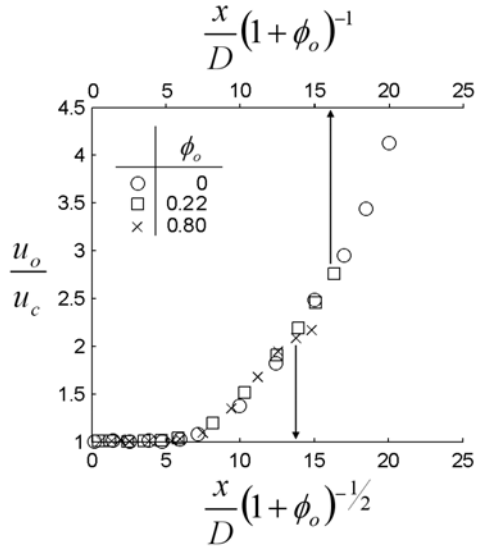

Figure 2.16: Gas phase centreline velocity as reported by Fan *et al.* (1997) but plotted as a function of $x/D(1+\phi_o)^{-1}$ for the case $\phi_o = 0.22$ and as a function of $x/D(1+\phi_o)^{-1/2}$ for the case $\phi_o = 0.8$. $St_o = 10$, $R^2_{xu}(n = 1, \phi_o = 0.22) = 0.97$, $R^2_{xu}(n = 0.5, \phi_o = 0.8) = 0.97$.

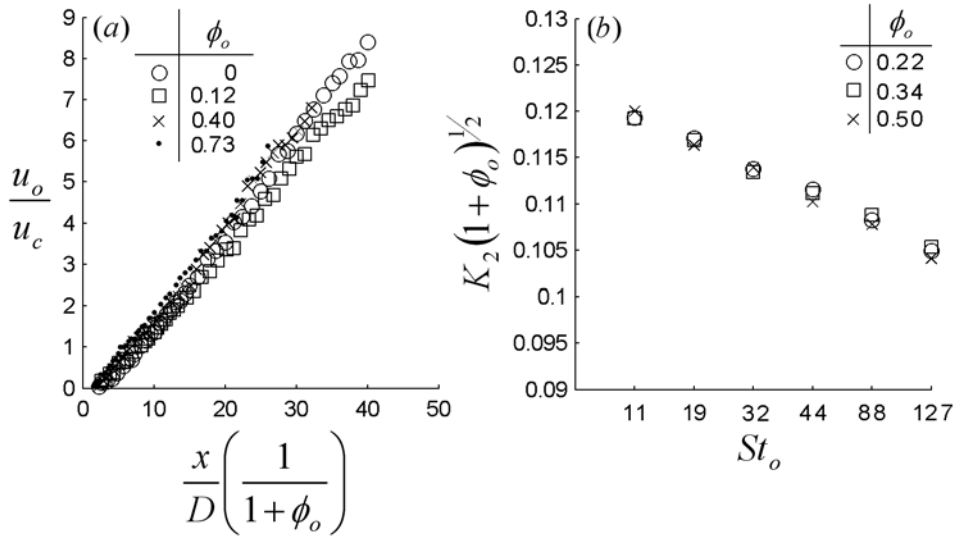

Figure 2.17: Gas phase centreline velocity (a) as reported by Ferrand *et al.* (2001), but plotted as a function of $x/D(1+\phi_o)^{-1}$ ($St_o = 18$, $R^2_{xr_{1/2}} = 0.98$, $\underline{R}^2_{xr_{1/2}} = 0.90$). Spreading coefficients, K_2, reported by Wall *et al.* (1982), but plotted as a function of $K_2(1+\phi_o)^{-1/2}$.

2.4 Power-law scaling of the solid phase and entrainment

Power law scaling functions similar to those presented in section 2.3 are next presented for measurements of the mass flux, concentration and entrainment.

2.4.1 Solid phase mass flux

The available reports of measurements of the solid phase mass flux support the hypothesis that the mass flux scales similarly to the gas phase velocity. The measurements considered here, performed by Laats and Frishman (1970), Wall *et al.* (1982) and Subramanian and Raman (1984), were all obtained with an isokinetic sampling technique (see section 1.5.2). Based on the gas phase velocity, the data of Laats and Frishman (1970) was found to

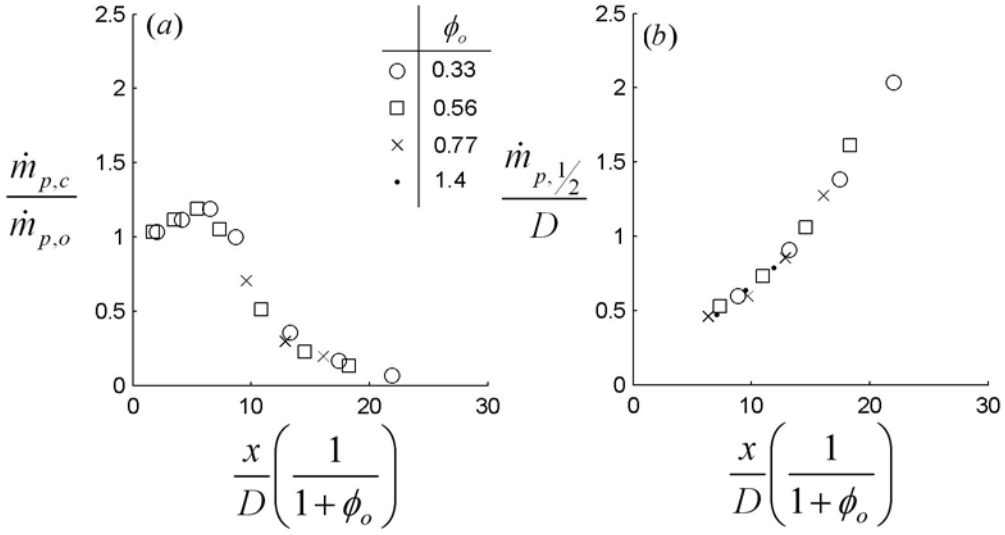

Figure 2.18: (a) Solid phase centreline mass flux, $\dot{m}_{p,c}$ normalised by the exit mass flux $\dot{m}_{p,o}$ and (b) mass flux half widths $\dot{m}_{p,1/2}$ as reported by Laats and Frishman (1970) plotted as functions of $x/D(1+\phi_o)^{-1}$ ($St_o = 18$).

be in the regime $St_o \lesssim 20$ while that of Subramanian and Raman (1984) is in the regime $St_o \gtrsim 200$. The regime of the data of Wall *et al.* (1982) is ambiguous. However, this is believed to be related to the different boundary conditions, i.e. the jet issues from a smooth contraction nozzle.

Solid phase centreline mass flux and half widths for the case $St_o = 18$ as reported by Laats and Frishman (1970) are shown to scale with $x/D(1+\phi_o)^{-1}$ in Figure 2.18, similarly to its corresponding gas phase data (see Figure 2.12a,b). Likewise, the centreline mass flux as reported by Subramanian and Raman (1982) scales satisfactorily with $x/D(1+\phi_o)^{-1/2}$ (Figure 2.19a). However, the case $\phi_o = 0.5$, does not collapse as well as the others.

For an assessment of half widths, the mass flux measurements as reported by Wall *et al.* (1982) are considered. Wall *et al.* (1982) report mass flux slopes, K, similarly to the velocity measurements presented in Figure 2.17(b) above. These (Figure 2.19b) are found to scale with $(1+\phi_o)^{-1/2}$. As discussed above, the flow of Wall *et al.* (1982) issues from a smooth contraction. The cases $St_o = 11$ and 19 are potentially in the regime where they may otherwise

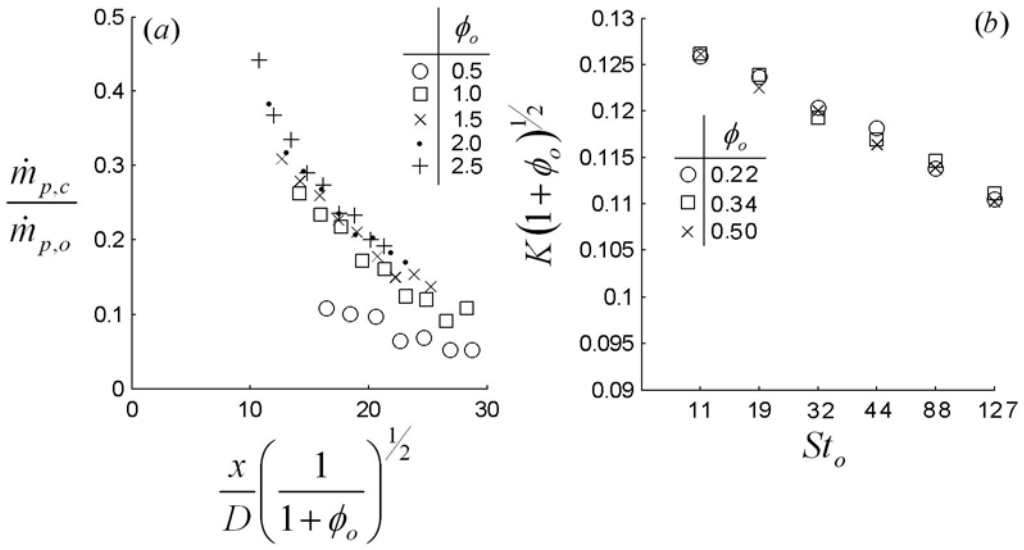

Figure 2.19: (a) Scaled solid phase centreline mass flux as reported by Subramanian and Raman (1984) for $St_o = 160$ and (b) half width slopes as reported by Wall *et al.* (1982), but scaled by $(1 + \phi_o)^{-1}$, for a range of St_o.

have scaled with $x/D(1 + \phi_o)^{-1}$, i.e. the low Stokes number regime. This might possibly be explained by the different inflow conditions. Wall *et al*'s jet was introduced through a smooth contraction which generates sufficiently more coherent motions than does a pipe jet (Mi *et al.*, 2001). These more coherent motions also lead to a greater rate of spread and decay in a smooth contraction jet than a pipe jet. Therefore, the characteristic time and length scales of the two classes of flow must be different, even with the same diameter and bulk exit velocity. Hence, the critical values of St_o which demarcate the regimes may be expected to differ between pipe jets and smooth contraction nozzles. However, further data is required to verify this hypothesis.

2.4.2 Solid phase concentration

It seems that the only measurement available from which to assess the scaling of the solid phase mass concentration (kg/m^3) are those by Ferrand *et al.* (2001), who report concentration half widths, $r_{1/2,c}$ for $St_o \approx 15$ in a jet issu-

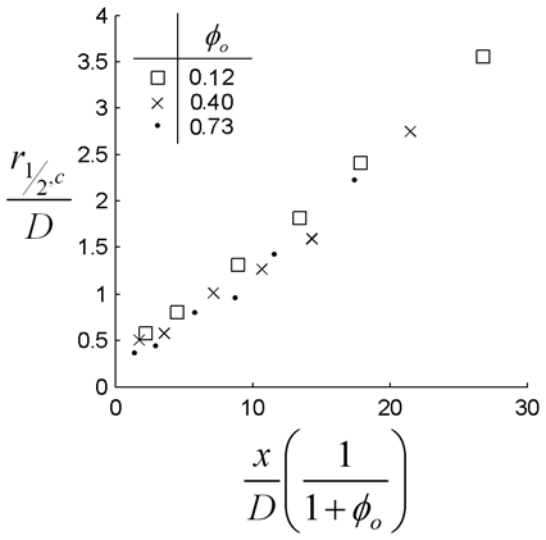

Figure 2.20: Concentration half widths as reported by Ferrand *et al.* (2001), but plotted as functions of $x/D(1+\phi_o)^{-1}$. $St_o = 15$

ing from a smooth contraction orifice. These are found to scale satisfactorily if plotted as a function of $x/D(1+\phi_o)^{-1}$ (Figure 2.20).

2.4.3 Entrainment

The work of Wall *et al.* (1982) and Subramanian and Raman (1984) drew on the earlier work of Field (1963), who originally studied the effect of the addition of particles on the entrainment of a turbulent axisymmetric jet. From Ricou and Spalding (1961), the entrainment of ambient fluid by single phase jets of a different density are related by the following relation:

$$\frac{\dot{m}_e}{\dot{m}_o} = K\frac{x}{D}\left(\frac{\rho}{\rho_o}\right)^{-1/2}, \tag{2.20}$$

where $\dot{m}_e$ is the entrained gas mass flow rate, $\dot{m}_o$ is the exit mass flow rate and K is some coefficient. For a particle-laden jet in which the density of transporting and entraining fluid is the same, $\phi_o = \rho(1+\phi_o)$ so that equation

2.20 becomes

$$\frac{\dot{m}_e}{\dot{m}_o} = K\frac{x}{D}\left(\frac{1}{1+\phi_o}\right)^{-1/2}. \tag{2.21}$$

Field (1963) provided values of Q_e/Q_o where Q is the volumetric flux and subscripts e and o denote the entrained and exit volumetric flow rate of gas respectively. Since the entrained gas has the same density as the exit gas in these data, then $\frac{\dot{m}_e}{\dot{m}_o} = \frac{Q_e}{Q_o}$ and thus

$$\frac{Q_e}{Q_o} = K\frac{x}{D}\left(\frac{1}{1+\phi_o}\right)^{-1/2}. \tag{2.22}$$

Figure 2.21 shows the entrainment data as reported by Field (1963) and Wall *et al.* (1982) respectively. These data collapse when scaled according to equation 2.22. For the high $St_o = 160$ data of Subramanian and Raman (1984), the collapse of data (not shown) is not as strong suggesting that equation 2.22 is valid only for relatively low St_o. A lower limit for equation 2.22 also exists based on the entrainment data for low St_o, as reported by Field (1963) and Wall *et al.* (1982) since for $St_o = 0.3$ and 1, the entrainment is found to *increase* with ϕ_o relative to the single phase case.

2.5 Conclusions

Exponential scaling factors that account for the effect of the exit mass loading on the gas phase centreline velocity and half width of a particle-laden jet were originally proposed by Melville and Bray (1979). However, the bulk of experimental data published since then suggests that the centreline velocity and half widths are scaled with a power-law factor. Three regimes have been identified from the data presented in Table 2.1:

- For low Stokes numbers $St_o \lesssim 20$, the gas phase centreline velocity and half width scale with $x/D(1+\phi_o)^{-1}$.
- For intermediate Stokes numbers, $20 \lesssim St_o \lesssim 200$, the gas phase

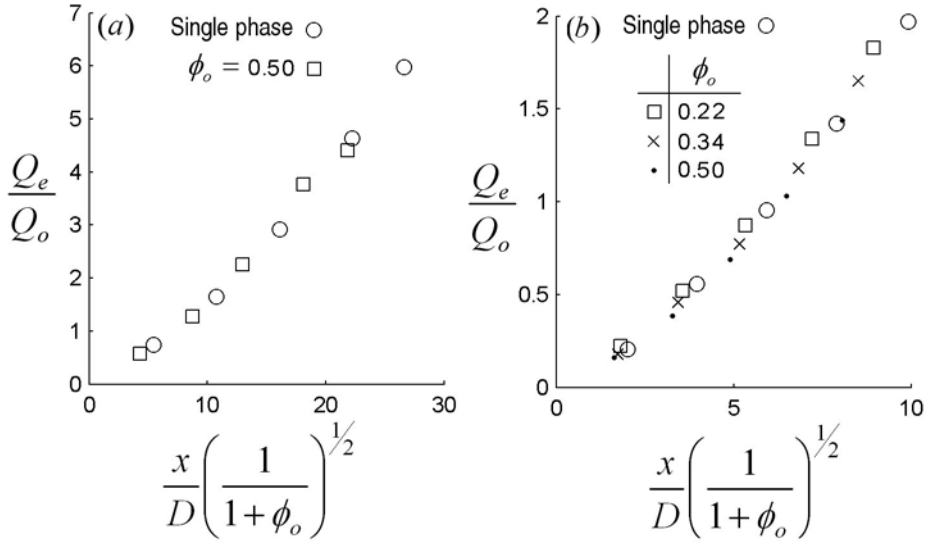

Figure 2.21: Entrainment measurements as reported by (a) Field (1963) (St_o = 5) and (b) Wall *et al.* (1982) (St_o = 45), but plotted as functions of $x/D(1+\phi_o)^{-1/2}$.

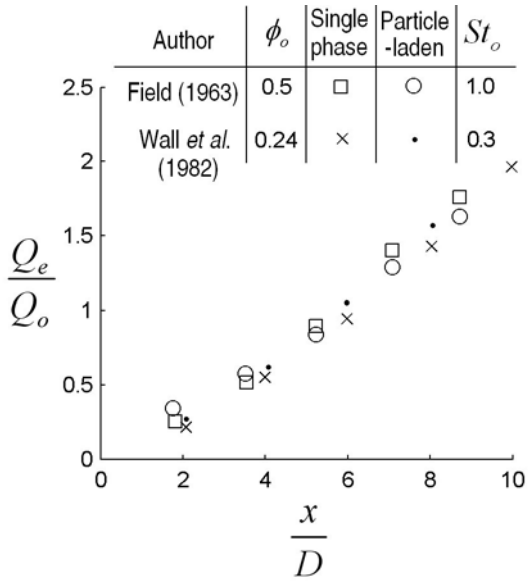

Figure 2.22: Entrainment measurements as reported by Wall *et al.* (1982) and Field (1963). An increase in entrainment is evident for an increase in ϕ_o at very low exit Stokes numbers ($St_o \lesssim 1$).

centreline velocity scales with $x/D(1+\phi_o)^{-1}$, and half width with $x/D(1+\phi_o)^{-1/2}$.

- For higher Stokes numbers, $St_o \gtrsim 200$, the gas phase centreline velocity scales with $x/D(1+\phi_o)^{-1}$, while the half widths are thought to be approximately independent of ϕ_o.

It is thought that these approximate regime boundaries may well depend on the boundary conditions.

In addition to the gas phase velocity field, power-law scaling factors for other particle-laden jet properties, such as the mass-flux, concentration and entrainment were found. Although this data is limited, it suggested that the solid phase mass-flux scaled similarly to the gas phase velocity. One concentration data set scaled with $x/D(1+\phi_o)^{-1}$ and two entrainment data sets scaled with $x/D(1+\phi_o)^{-1/2}$.